
A tale of two transforms: 3D raypath interferometry

David C. Henley

ABSTRACT

The heart of the near-surface correction technique known as raypath interferometry is the transform (and its inverse) used to move standard field seismic data from the conventional X/T domain to a raypath-oriented domain, and back to the X/T domain. We have extensively tested two different transforms for this purpose; the Radial Trace Transform, a simple point-to-point mapping, and the Tau-P Transform, an integral transform. We show here that, while either transform can be used on 2D seismic data, for the 3D case, geometrical considerations favour the Tau-P Transform, since the current Radial Trace algorithm does not properly handle seismic survey geometry. The Tau-P Transform is not without problems, however, the most serious being the massive storage required for transforms whose parameters are chosen to properly preserve the lateral resolution of the input data. We illustrate the issues here using the 1995 Blackfoot 3D 3C data set and show images of the successful application of raypath interferometry to both the PP (vertical) and PS (radial) components of this data set.

INTRODUCTION

Raypath interferometry was developed as a method for correcting seismic reflection data for the effects of a complex and/or irregular near-surface layer, particularly in those regions where conventional statics techniques fail. The technique is especially attractive for use on converted wave data, since it derives and applies corrections along the raypath direction, thus enabling the nonstationary corrections required for most shear waves (Cova et al, 2013a, 2013b, 2014a, 2014b, 2014c).

The primary motivation behind the development of raypath interferometry was the failure of conventional static corrections to properly correct reflection seismic data for near-surface effects in particular physical scenarios, like high-velocity surface layers and significant near-surface velocity contrasts (leading to scattering of reflection arrivals) (Henley, 2008, 2012a, 2012b). Since conventional correction methods rely on the assumption of low-velocity surface layers (surface consistency) and single, uncomplicated reflection wavefront arrivals, it is no surprise that these methods either fail completely or produce unsatisfactory results. In addition, Cova et al (2013a, 2013b, 2014a, 2014b, 2014c) showed from first principles that corrections for shear wave arrivals are nonstationary by nature (time-varying static shifts required), and that surface-consistency is usually an inappropriate assumption. Hence, raypath interferometry introduces two key ideas intended to replace the surface-consistency and single-arrival assumptions used in conventional near-surface correction techniques: the more general *raypath-consistency assumption*, and the *wavefront arrival distribution* (surface function) assumption.

Raypath consistency

For much of the seismic reflection data acquired on land, the surface layer of the earth is a soft, weathered zone of soil and under-compacted sediments whose velocity is

considerably lower than the first competent rock layer in the subsurface. In this instance, Snell's Law compels seismic energy transmitted into the deeper subsurface layers to travel along a nearly vertical raypath from the source through the first rock interface, and nearly vertically back from this interface to a receiver, regardless of the actual reflection point for the energy (Figure 1). This means that the time delay for wavefronts passing through the surface layer at a particular surface point is nearly constant for all possible raypaths originating or terminating at that surface point; this is the so-called surface-consistency assumption. When velocity in the surface layer is higher relative to the underlying layers, however, we see that the wavefront delay through the surface layer depends upon the reflection point, and hence the raypath (Figure 2). In this case, however, we can reconfigure the input data to collect all raypaths with a common incidence angle and surface location, as in Figure 3, and then constrain the wavefront time delay through the surface layer to be the same for all raypaths *with a common near-surface segment*; this is the raypath-consistency assumption (of which the surface-consistency assumption is a limiting case). The key to exploiting this assumption is in the reorganizing of the input seismic data to correspond to the raypath diagram in Figure 3. It is shown elsewhere that transforming the input seismic data from the X/T domain either to the Radial Trace (RT) domain (Henley, 2008, 2012a, 2012b) or to the Tau-P domain (Cova et al, 2014c, 2015a, 2015b, 2016, 2017) and sorting by common ray-parameter accomplishes this step and presents the data in an arrangement convenient for deriving and applying correction operators.

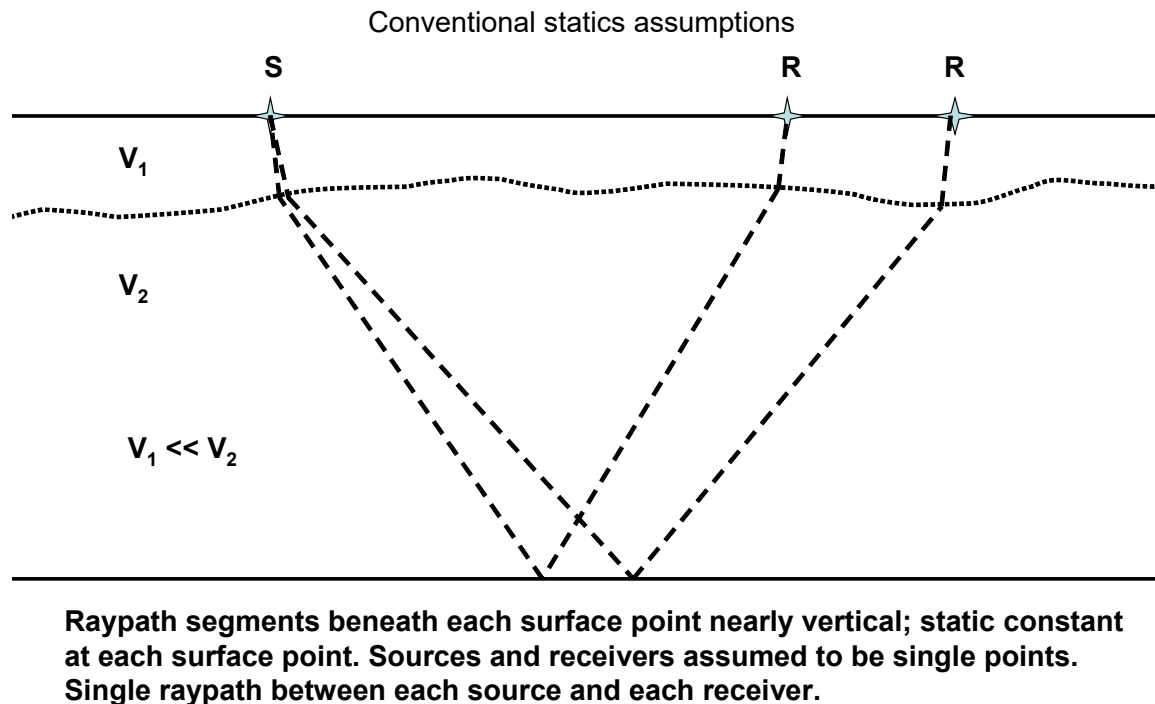
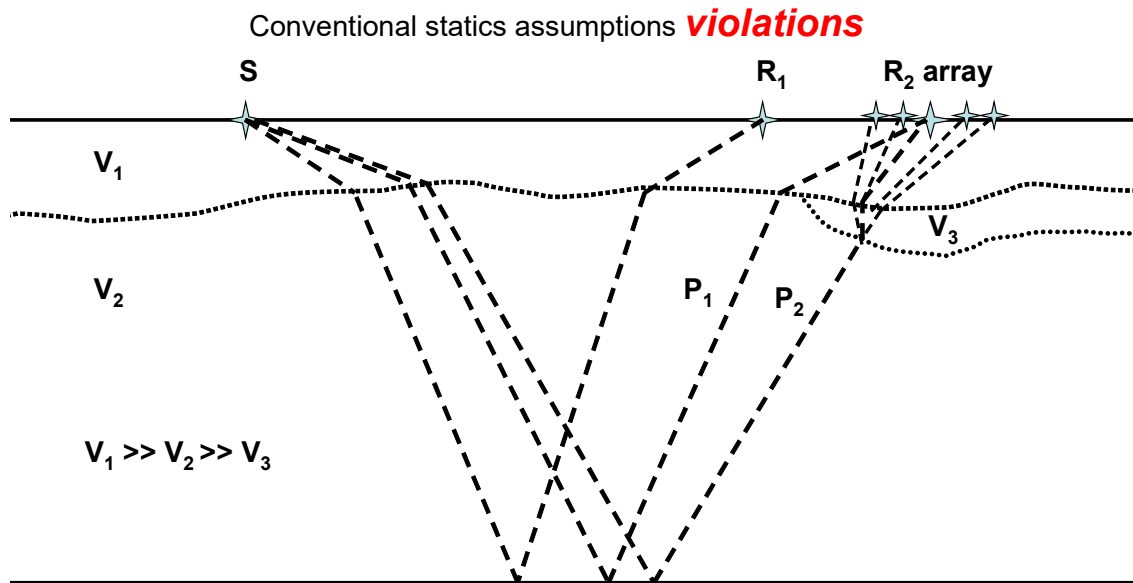


FIG. 1. When the velocity of the near-surface layer is less than that of the underlying bedrock, raypaths through the layer are nearly perpendicular, and therefore nearly independent of reflection points in the subsurface.



Raypath segments beneath surface points not vertical; no common static at each surface point Sources and receivers can be arrays, with different statics for each surface point in the array. Multiple raypaths possible between each source and receiver location (P_1 and P_2), due to buried velocity anomalies (V_3)

FIG. 2. When the velocity of the near-surface layer exceeds that of the bedrock, raypath segments in that layer are no longer nearly vertical, and depend directly on the location of reflection points in the subsurface.

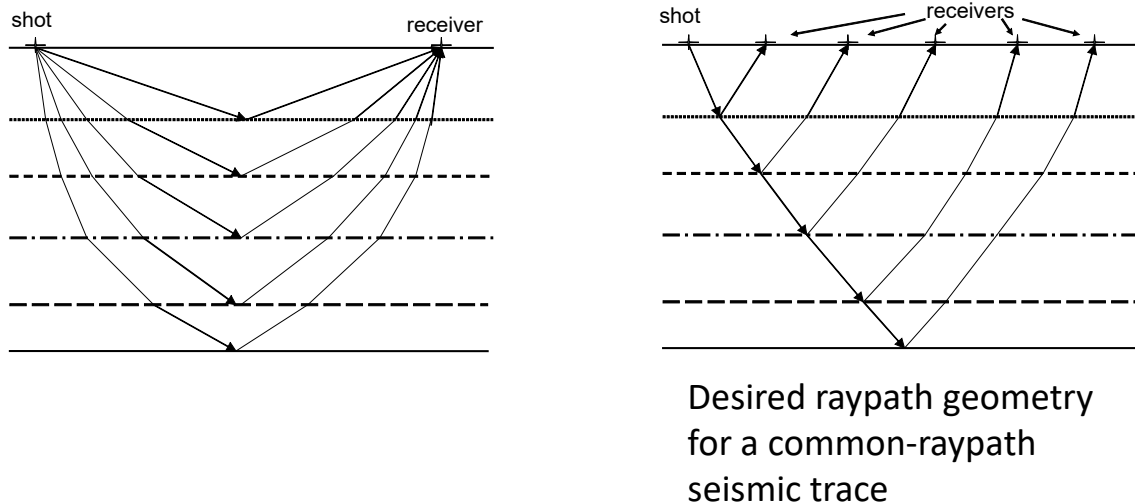


FIG. 3. Raypath geometry of a conventional seismic trace (left) must be converted to the geometry of a common-raypath seismic trace by a transform of the input X/T trace gathers.

Surface function

When the surface layer is relatively homogeneous, corrections to reflection seismic data for the presence of the layer can be applied simply by time-shifting seismic traces

(either conventional X/T traces or transformed common-raypath traces) by an amount equal to the transit time of a single reflection wavefront through the layer at each surface point, the so-called ‘static’ correction. The assumption behind this procedure is that there is only a single arrival from any reflection wavefront at the surface, and that there is no uncertainty in its arrival time; in other words, the arrival corresponds to the waveform of the reflection event convolved with a time-shifted unit spike at the position of the static shift. If the surface layer is not homogeneous, however, and contains prominent layering or pods of material from which reflection wavefronts can scatter, secondary arrivals from internal multiples and/or scattered events may accompany the primary wavefront arrival. The arrival packet then corresponds to the reflection waveform convolved with a distribution of spikes, of which the largest is usually at the time of the overall static shift. If there is any uncertainty in the arrival time of the principle reflection arrival (due to noise or signal bandwidth), this uncertainty may contribute to broadening of the arrival distribution. We call this broadened arrival distribution a ‘surface function’, since it characterizes the propagation of any reflection wavefront through the surface at a particular location (and along a particular raypath). While a single spike surface function can be removed from a trace by a simple time shift, a distribution of spikes can only be removed by estimating the distribution shape and deconvolving it. The process we use for estimating the shape of each surface function for every surface location and raypath angle and subsequently removing it from the data is the raypath interferometry technique.

Interferometry process

Figure 4 illustrates the optical analog of the interferometric process that we use for raypath interferometry. A key step in this process is the estimation of the ‘reference wavefield’, which consists of a zeroth order estimation of the wavefield as it would appear had it not encountered near-surface irregularities. A key finding of our ongoing research is that a wide variety of techniques can be used to estimate this reference wavefield, including trace mixing and eigenvector filtering (Henley, 2014c) applied to raw trace gathers of whatever sort are being used to derive and apply corrections. If we were to use the interferometry technique to derive and apply surface functions to seismic data in the X/T domain, then common-source gathers and common-receiver gathers would be the trace ensembles of choice for estimating the reference wavefield. Since we use the raypath domain, however, our ensemble of choice is the common-ray-parameter trace gather, and it is this to which we apply the trace mixing and/or eigenvector filtering to estimate the reference wavefield.

After the reference wavefield estimation step, we then have pairs of ensembles with which to perform the interferometry, a reference ensemble and corresponding raw data ensemble for every value of the ray-parameter. We cross-correlate each trace in the raw ensemble with its corresponding trace in the reference ensemble, then ‘condition’ each cross-correlation function by raising its samples to an odd integer power and windowing the function with a Hanning function. We consider these ‘conditioned’ cross-correlation functions to be our estimated surface functions, and we remove them by either deriving an inverse filter for each and applying the inverse filter to the appropriate raw trace, or by cross-correlating each ‘conditioned’ correlation function, as a match-filter, with its corresponding raw trace. Figure 5 shows a typical common-ray-parameter gather before correction and after the interferometry procedure. After all the common-ray-parameter

ensembles for a seismic survey have been subjected to the interferometry step, they are re-sorted and inverse transformed back to the X/T source gather domain for imaging. Figures 6 and 7 show an example of raypath interferometry applied to converted wave data from Hussar, Alberta. Interestingly, the corrections have improved event continuity over the entire section, unlike the conventional processing shown in Figure 8, where the main improvements occur deeper in the section, rather than in the shallow portion, and the events appear to be limited in bandwidth. The effectiveness of nonstationary corrections for these data is thus suggested by the results in Figure 7.

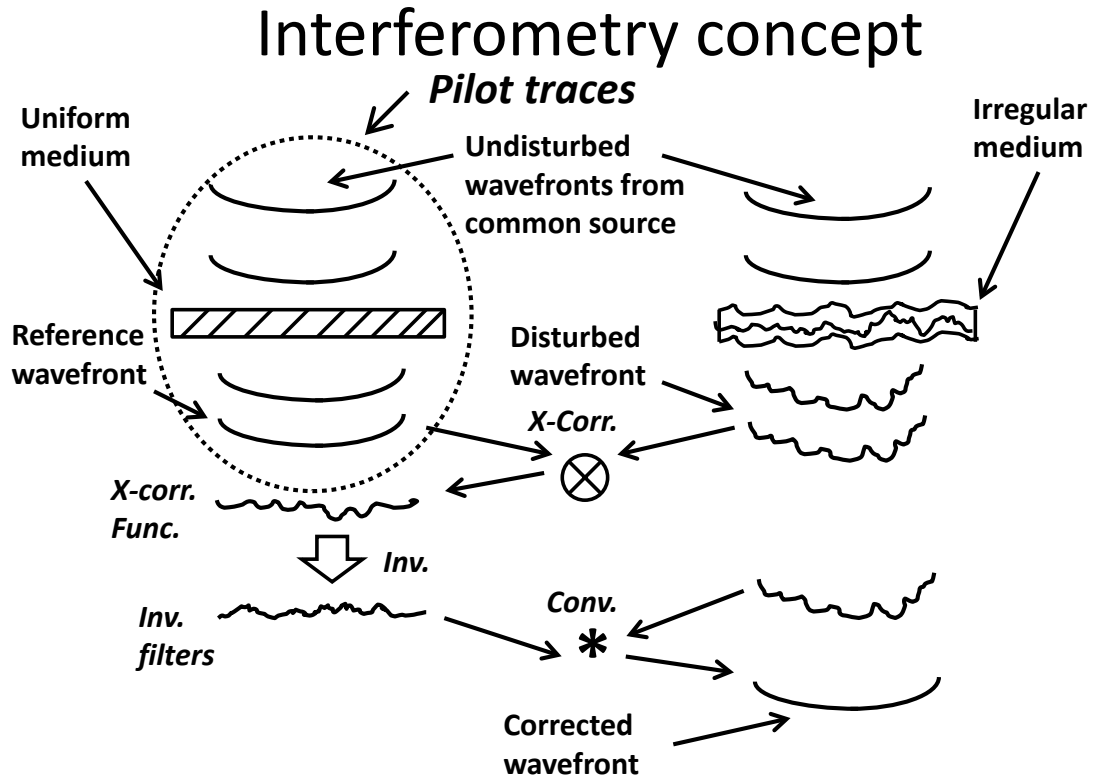


FIG. 4. Schematic illustrating the interferometric concept used in raypath interferometry. A key step is creating the 'reference wavefield', otherwise known as 'pilot traces'.

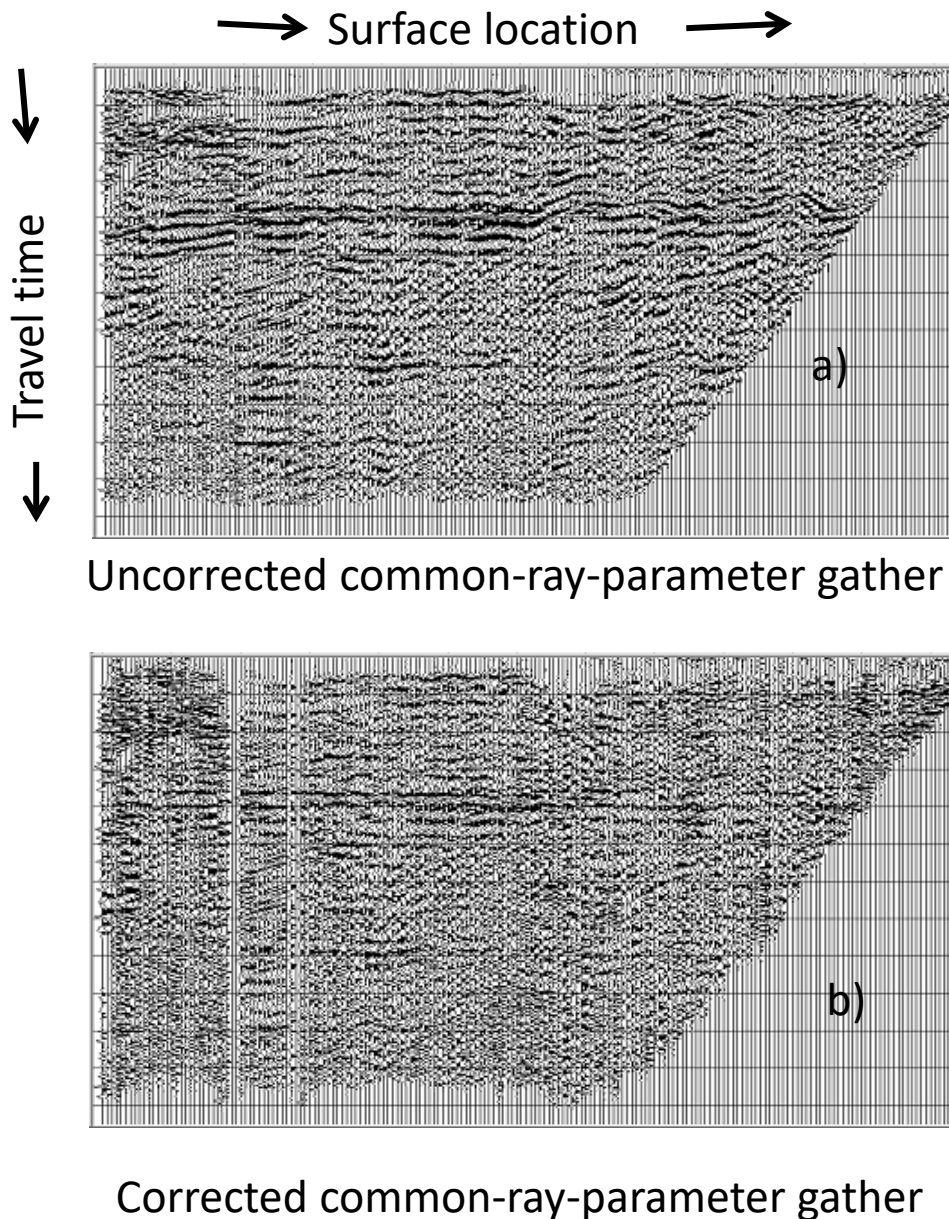
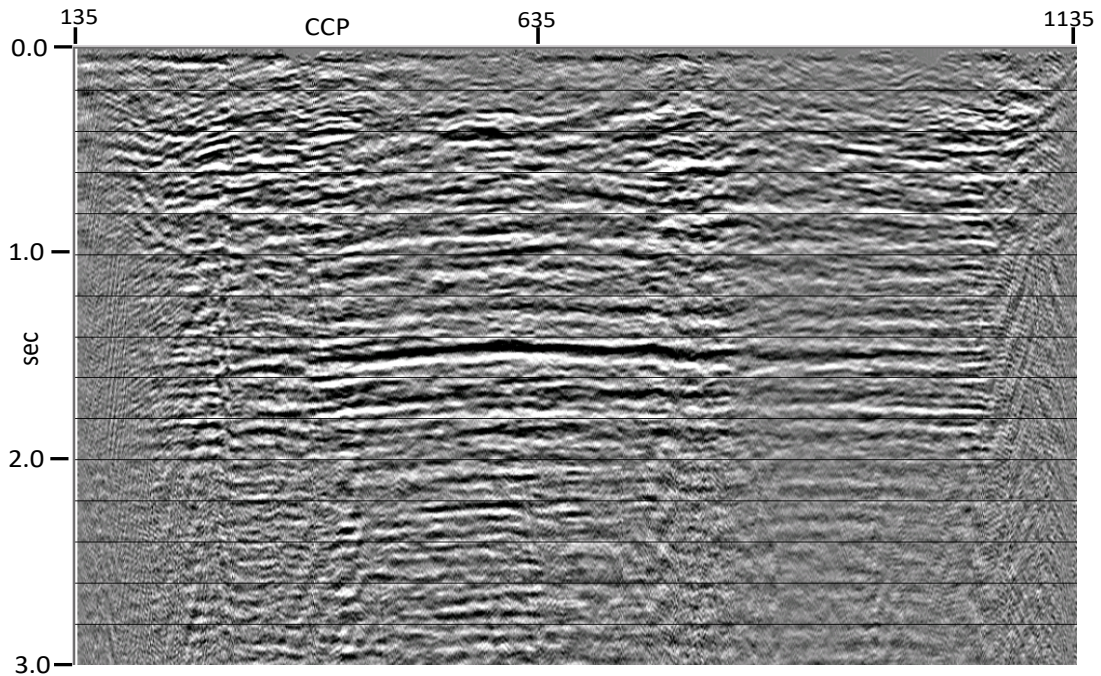
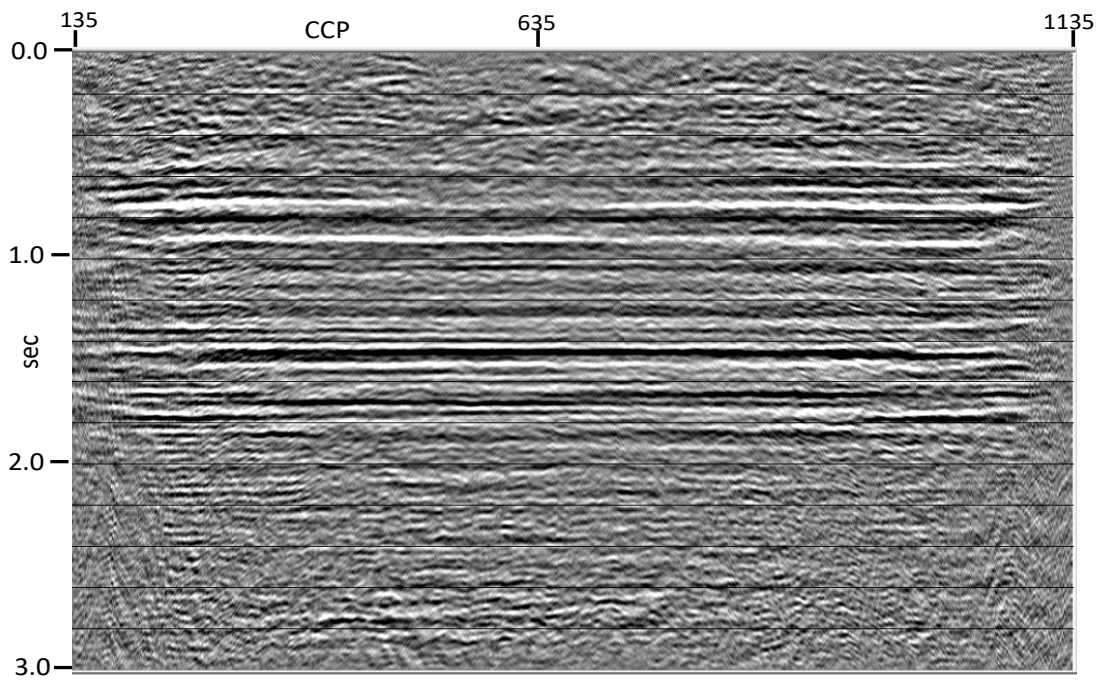


FIG. 5. After transforming to the source/raypath domain (in this case the Radial Trace or RT domain), traces have been sorted into common-ray-parameter gathers, where velocity or slowness is the ray parameter. Each common-ray-parameter gather a) is correlated against its corresponding common-ray-parameter reference wavefield gather, and the resulting conditioned correlation functions are then used to correct the original common-ray-parameter gather b). The corrected common-ray-parameter gathers are then re-sorted to raypath/source gathers, which are finally transformed back to the X/T domain.



Brute CCP stack of Hussar radial component

FIG. 6. CCP stack of radial component traces from the Hussar experiment with single NMO function and no statics applied.



CCP stack of Hussar radial component after raypath interferometry—single NMO function

FIG. 7. CCP stack of Hussar radial component with single NMO function after raypath interferometry. Coherence and flatness of events improved for the full range of travel times. Spectral bandwidth also well-preserved.

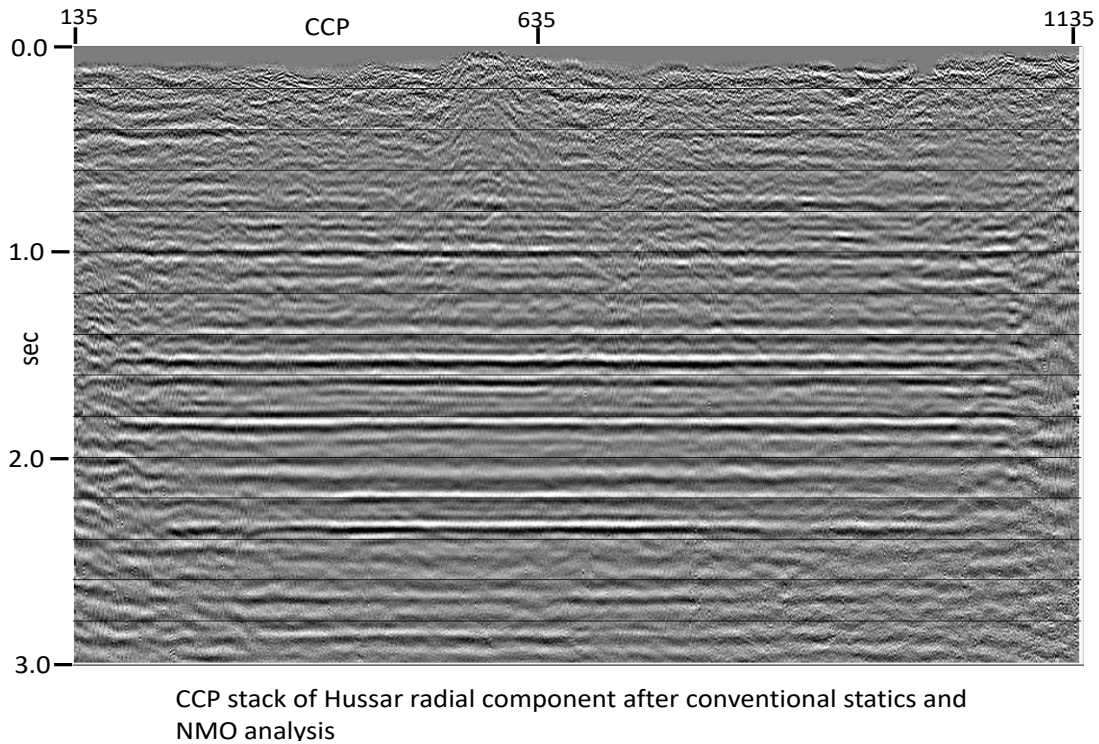


FIG. 8 CCP stack of Hussar radial component with laterally varying NMO and conventional statics. Shallow events faint and discontinuous; all events appear relatively narrow in bandwidth.

The transform

RT Transform

The key step in raypath interferometry is transforming the seismic reflection data from the usual X/T domain in which they were recorded to a ‘raypath’ domain; then transforming them back after corrections are applied. In all early work, the Radial Trace Transform (Claerbout, 1983) was used because of its simplicity, and the fidelity of its inversion; it can be exactly inverted, depending upon the interpolation chosen and the oversampling determined by the input parameters. The specific algorithm written by us for ProMAX (SeisSpace) was designed specifically for 2D acquisition geometry, including traces whose source-receiver offset values are linearly distributed along the surface (Henley, 1999). It does not preserve trace header information explicitly, as do most commercially supported transform algorithms. The transform and its inverse are simply formulas which map each sample from the X/T domain to one or more samples in the RT domain (where one dimension is a ray parameter), and vice versa. Interpolation is a necessary part of the transform and its inverse, since the sample distribution in one domain is not uniform relative to the sampling in the other domain. Using ‘nearest neighbor’ interpolation makes the transform and its inverse exact; but using an l^p -norm weighted interpolation with a relatively large value of p makes the transform/inverse nearly exact, while protecting against artifacts introduced by processing in the RT domain and amplified by the inverse transform. Although the RT Transform usually requires more storage than the original X/T data gather in order to preserve lateral detail, it is usually no more than 2-5 times the size of the original data gather.

Tau-P Transform

The Tau-P transform is a form of the Radon Transform (an integral transform similar to the Fourier Transform) adapted for use on seismic data, and has the same guarantee of invertibility, as long as the number of forward projections in the transform is infinite, and the projections cover a 360deg aperture. Hence, when reduced to finite summations and limited apertures, the Tau-P transform is only imperfectly invertible, depending upon the aperture limits and the number of projections within the aperture. Cova et al (2014c, 2015a, 2015b, 2016, 2017) showed that the Tau-P Transform and its inverse can be made precise enough, with careful parameter choice, to preserve enough fidelity in the input data, within the bandlimits of the data, to support at least one forward/inverse operation. They also demonstrated that the Tau-P transform, with its slowness P as the ray parameter, is a more natural choice for transforming seismic data to a ray-parameter domain. In addition, commercially supported Tau-P algorithms make no assumptions about source-receiver offset value distribution, but carry all trace header information through forward and inverse operations, a big advantage for irregular/unusual trace distributions. On the other hand, when the parameters for the Tau-P transform are chosen to preserve lateral details in the input data comparable in scale to one trace increment, the storage requirement for the resulting Tau-P transform is often 100 times or more the size of the original X/T gather.

3D considerations

Surface functions

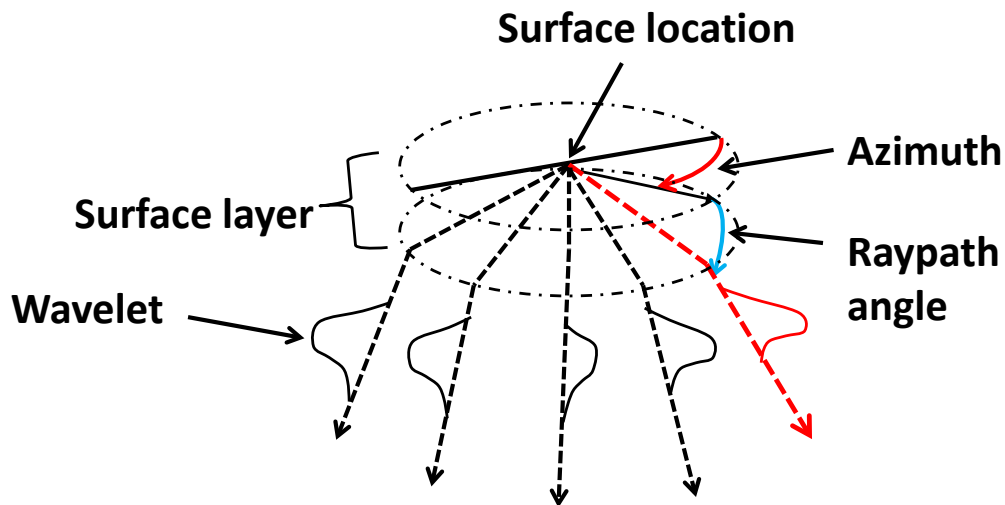
An obvious way to extend raypath interferometry into 3D is to begin by expanding the 2D surface function concept to 3D by adding an additional independent variable, in this case, source-receiver azimuth (Henley, 2015, 2016a, 2016b, 2017). Figure 9 illustrates the concept of a surface function, whose waveform (arrival distribution function) varies with surface location, raypath angle, and source-receiver azimuth.

Seismic data geometry

In order to use seismic data to estimate and apply surface functions in 3D, we need to be able to create trace ensembles with coordinates connected to those of the 3D surface functions. Since 3D seismic surveys are usually acquired with Cartesian (rectangular) coordinates, we need to create new trace headers containing source-receiver azimuth for each trace, as well as signed source-receiver offset (sign indicates relative positions of source and receiver). When we select trace ensembles by common shot, common azimuth (or azimuth bin), and ascending source-receiver offset, we then have the required input for a transform to the ray-parameter domain. Unfortunately, the relatively regular Cartesian coordinates of the acquisition sampling do not map to uniform sampling in the wedge-shaped common-azimuth bins (Figure 10), and we must choose the dimensions of the common-azimuth bins (by trial and error) to simultaneously optimize the trace population and offset distribution within each bin. In order to use either the RT or the Tau-P transform (which are essentially 2D transforms), we need to keep the azimuth bins as narrow as possible, to ensure that the traces approximately lie in a 2D plane through the data volume. Figure 11, however, shows what happens if we choose the bin width too narrow (3deg); the majority of the bins contain too few traces to yield a meaningful RT or Tau-P transform. Widening the bins in angle means relaxing the requirement for coplanar

traces as input to the transforms, but it helps create bins with a larger trace population, as well as a more uniform distribution of source-receiver offsets. Figure 12 shows the traces for one source gather as collected into bins subtending 30deg. Here, the majority of the traces in the source gather are collected into groups suitable for transforming. Even here, however, there are a few bins with too few traces. By creating ‘super-bins’, each consisting of two co-planar bins separated by 180deg, we can create azimuthal bins which are populated densely and uniformly enough to transform reliably (Figure 13). In this binning arrangement (Figure 14), each group of traces corresponding to a constant azimuth bin (red over-plot) are transformed independently, as in Figure 15, where the common-azimuth gathers for a single source have been transformed to the RT domain.

3D surface function



Wavelet is the time distribution of reflection arrivals and depends upon surface location, azimuth, and raypath angle

FIG. 9. Schematic illustrating the 3D surface function that we need to determine for every surface location in order to deconvolve it from traces sharing that surface location.

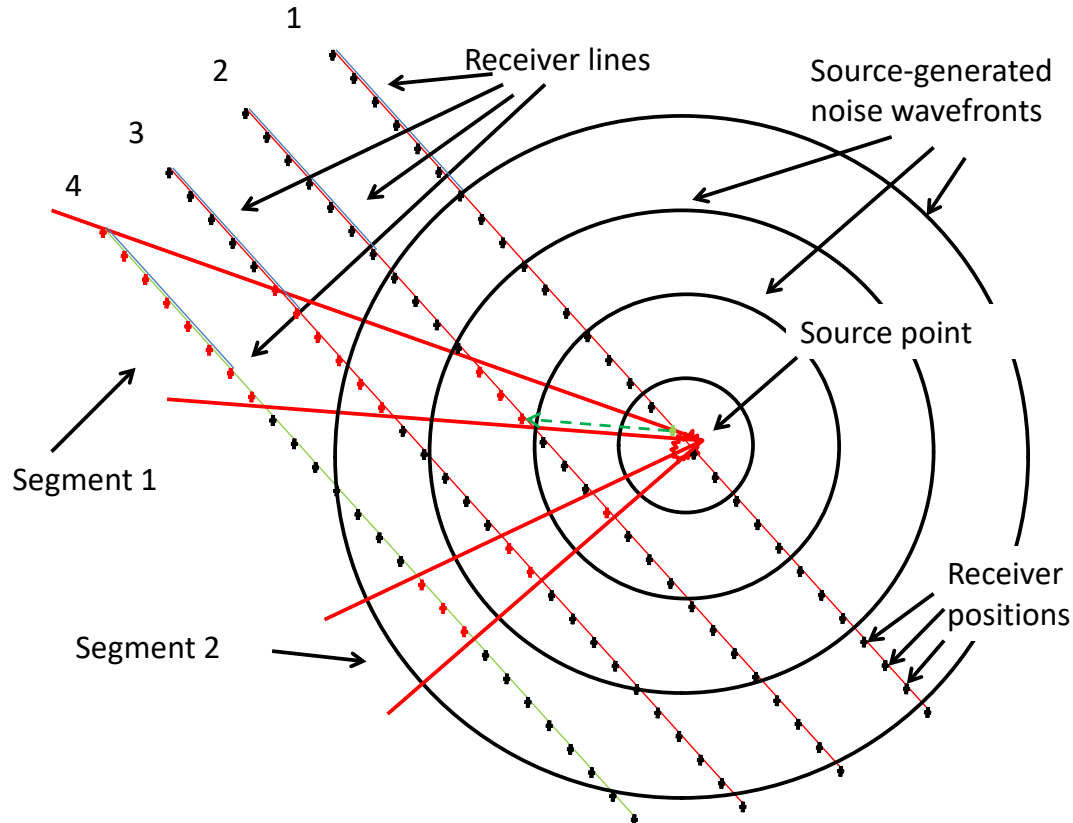
Test data

In order to test various 3D raypath geometry concepts, we needed a 3D field data set with the following characteristics:

- Multi-component data with uniform subsurface coverage.
- Relatively regular acquisition geometry.
- Good quality seismic data with significant apparent surface (static) corrections required.

- Modest survey size (approx. 10^6 traces/component) to keep processing effort reasonable.

Fortunately, our 1995 Blackfoot 3D 3C survey (Simin et al, 1996) satisfied all of these requirements, and has been used for all subsequent testing (Henley 2015, 2016a, 2016b, 2017). All real data shown henceforth belong either to the PP (vertical) or the PS (inline radial) components of this data set.



If traces are gathered by source-receiver offset within angular segments, trace offset distributions will vary widely in range and uniformity with segment choice

FIG. 10. Schematic illustrating why source-receiver offset values are irregularly distributed within azimuth segments, when conventional 3D seismic acquisition geometry is used.

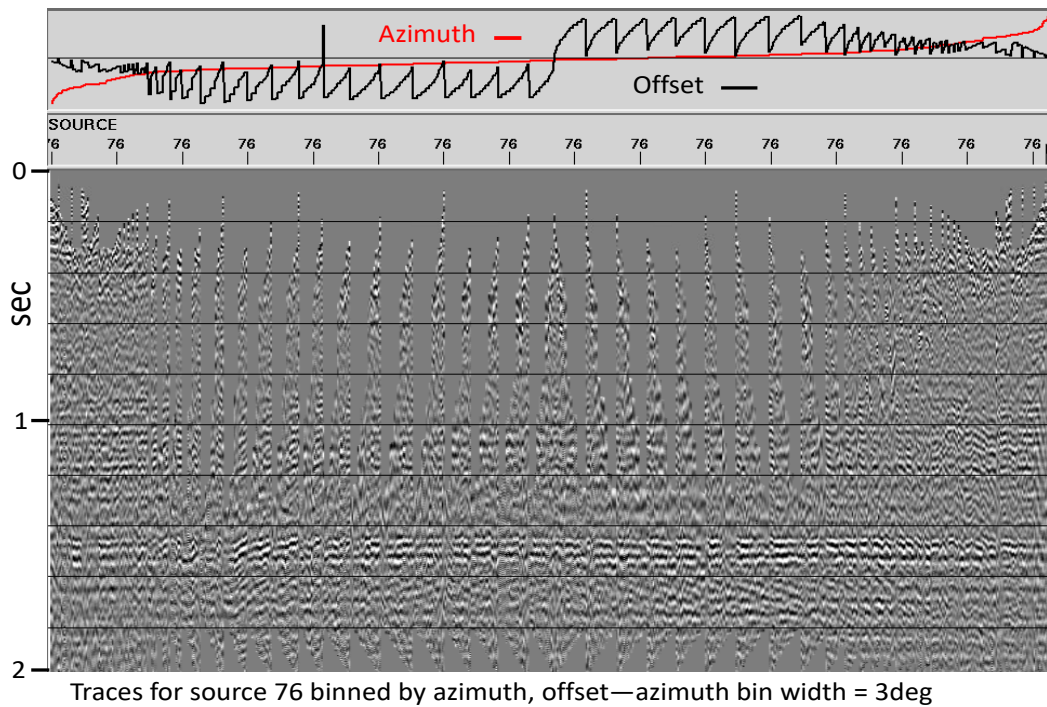


FIG. 11. Vertical component traces for Blackfoot source 76 binned by azimuth. When azimuth bins are too narrow (in this case, 3deg), many bins contain too few traces for proper analysis, and offset distributions (black plot) are mostly irregular.

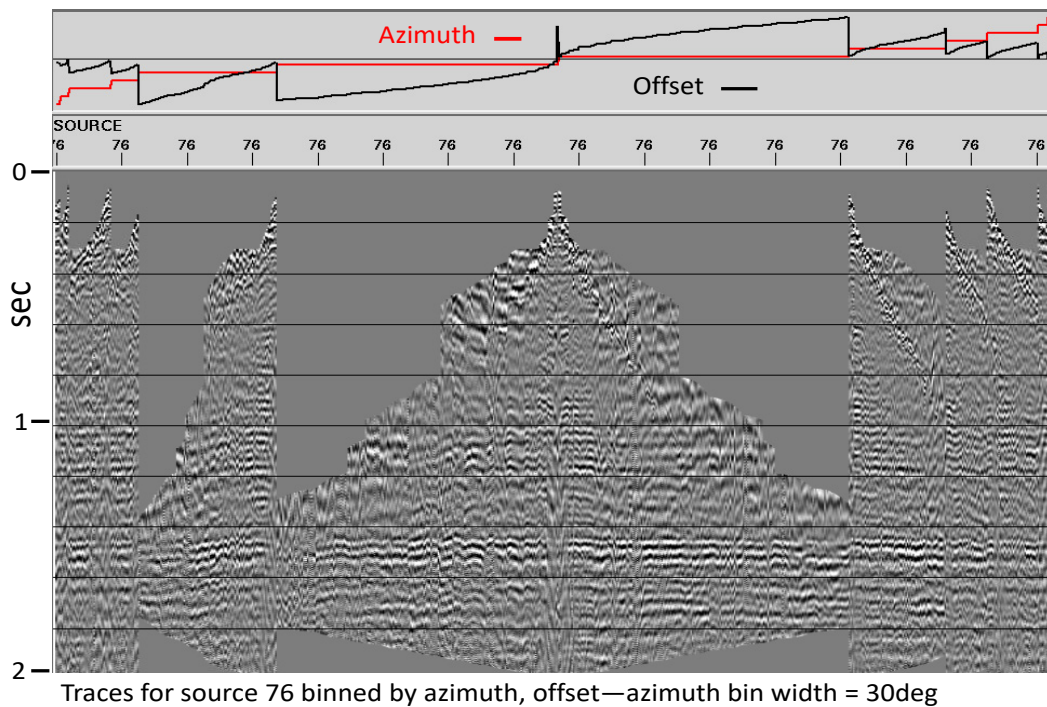
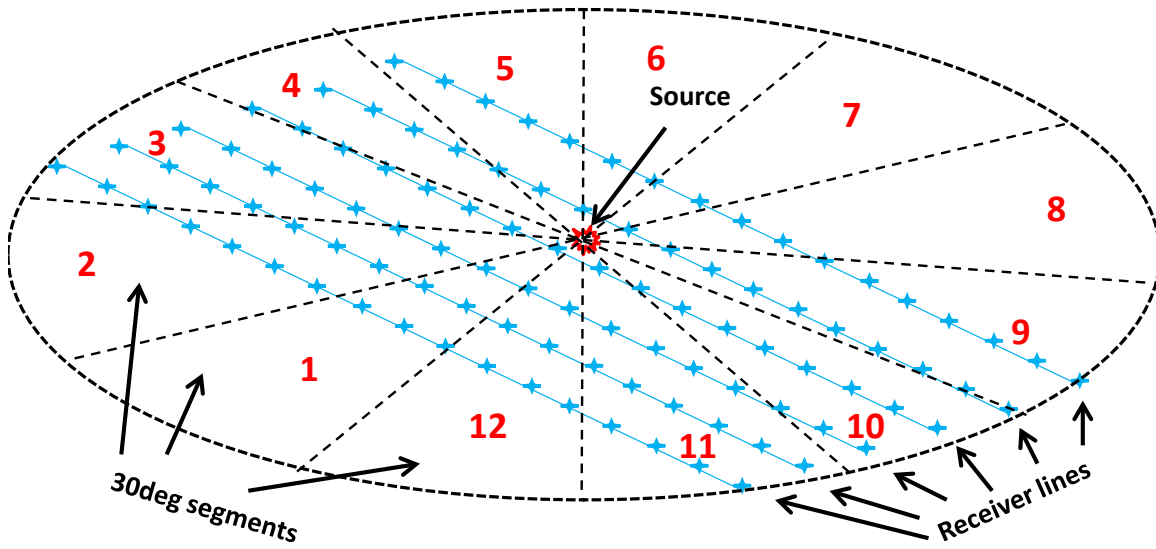
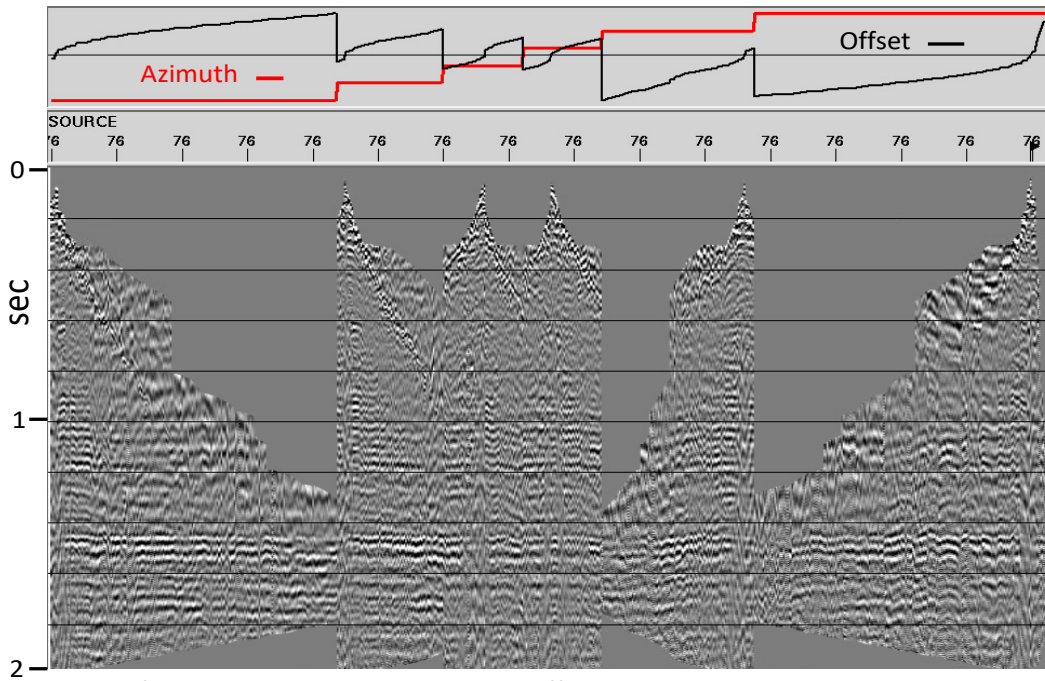


FIG. 12. Vertical component traces for Blackfoot source 76 binned by azimuth. Wider azimuth bins (in this case, 30deg) are better populated and have more linear offset distributions, but some bins still contain too few traces.



Bins consist of segments 1 + 7, 2 + 8, 3 + 9, 4 + 10, 5 + 11, and 6 + 12

FIG. 13. Schematic showing a binning scheme wherein azimuth bins aligned at 180deg are combined, since they're approximately coplanar. With this scheme, bins are adequately populated, and offset distributions are *relatively* linear.



Traces for source 76 binned by azimuth, offset—azimuth bin width = 30deg, bins aligned by 180deg appended

FIG. 14. Vertical component traces for Blackfoot source 76 binned using the scheme in Figure 13. These bins are adequately populated, and offset distributions *relatively* linear.

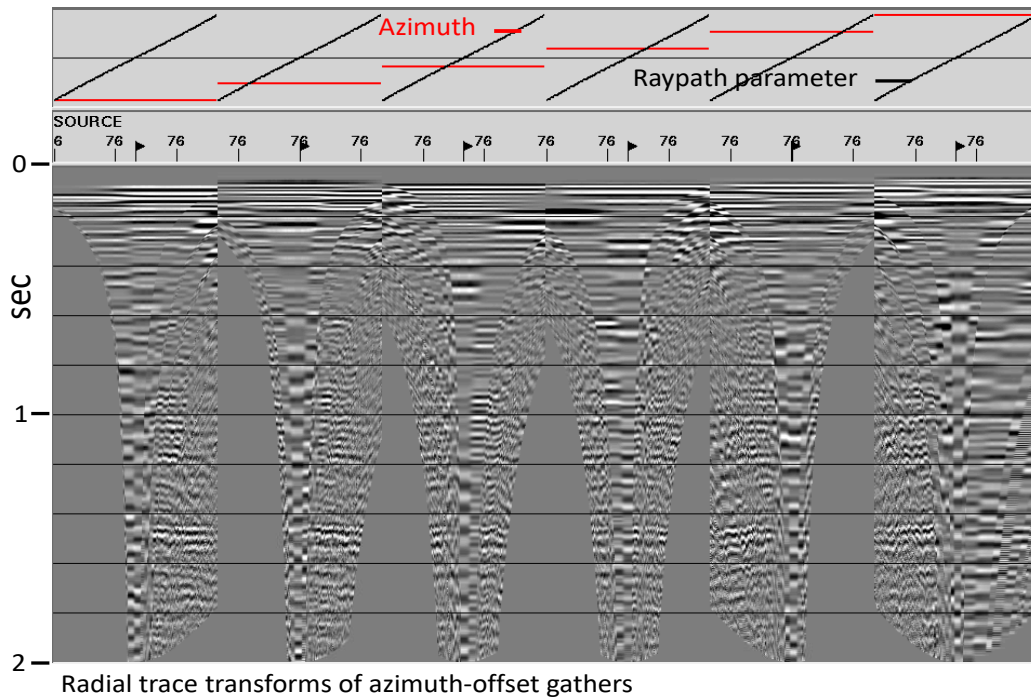


FIG. 15. The traces in each azimuth bin in Figure 14 have been transformed to the radial trace (RT) domain, the first step in raypath interferometry.

3D raypath interferometry—RT Transform

3D wavefield estimation and interferometry application—PP

In 2D raypath interferometry, we sort the RT (or Tau-P) transformed data by raypath parameter and surface location into common-ray-parameter gathers. The estimated wavefield for each common-ray-parameter gather is then created by flattening, laterally smoothing the traces of each gather, and unflattening. The smoothing can be ordinary trace mixing, or eigenvector filtering; the results are not sensitive to the choice of technique. For 2D data, the smoothing is carried out in one dimension (surface location), since the surface functions derived during 2D raypath interferometry are confined to the single plane defined by the acquisition parameters.

For 3D, however, the estimated wavefield has one more dimension; so the common-ray-parameter trace ensembles must be smoothed in two dimensions, rather than one. The common-ray-parameter ensembles can be sorted either by azimuth and source, as in Figure 16, or by source and azimuth, as in Figure 17. It should be noted that these dimensions are not linearly independent; but for the purposes of data smoothing, this seems not to be important. Figure 18 shows a common-ray-parameter ensemble smoothed in both dimensions to form the estimated wavefield for the common-ray-parameter gather shown in Figure 16. Each trace in the estimated wavefield is cross-correlated with the corresponding trace from the raw (unsmoothed) common-ray-parameter gather, and the resulting cross-correlation functions used to create filters to apply surface corrections to each trace of the common-ray-parameter gather, as in Figure 19. All the corrected common-ray-parameter gathers can be re-sorted into source/azimuth/raypath gathers

(Figure 20), and inverse-transformed back to source/azimuth/offset gathers as in Figure 21.

The RT Transform problem

When we compare the corrected source gather in Figure 21 with the raw source gather in Figure 14, we immediately see that something is wrong; the offset distributions plotted at the top of Figure 21 are linear, whereas those in Figure 14 are only approximately linear. The inverse RT Transform does not return the original offset values to the traces, but only linearly interpolated offsets (Henley, 1999). While this generally works for 2D data, where source-receiver offsets are nearly always linearly distributed, it fails for 3D data, where the source-receiver offsets are only truly linear when the source is collinear with the receiver line. Hence, while we can compare plots of the same source ensemble before and after raypath interferometry (Figures 22 and 23), and we can see that the reflections are flatter and more coherent after the interferometry, we cannot continue to the next step, NMO correction and CMP stack because of the inaccurate geometry.

Interferometry application—PS

For converted wave (PS) data, we can follow the same general technique as for PP data; create an estimated wavefield, correlate the wavefield with the raw common-ray-parameter traces, derive and apply inverse filters, and sort and transform the data back to PS source gathers. Figure 24 shows an uncorrected common-ray-parameter gather next to the same gather after raypath interferometry. The improvement in event coherence is obvious. However, when we sort and transform back to PS source gathers, as in Figure 25, we observe the same offset distortion as with the PP data, and we can proceed no further.

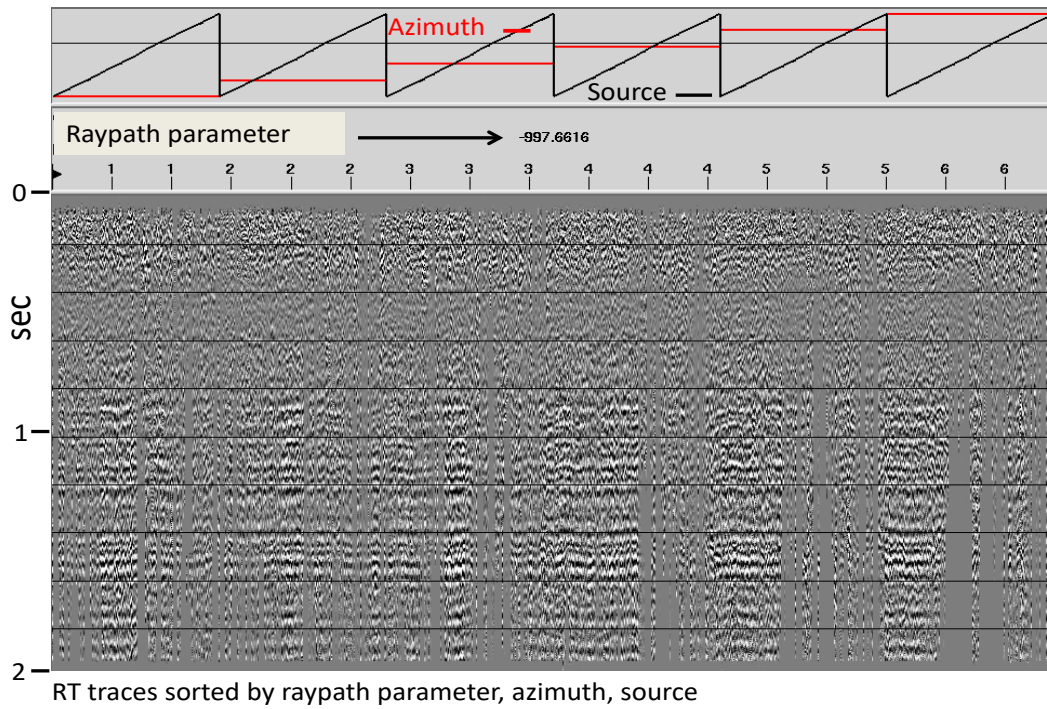


FIG. 16. Vertical component Blackfoot traces for one common-ray-parameter panel sorted by azimuth, then source.

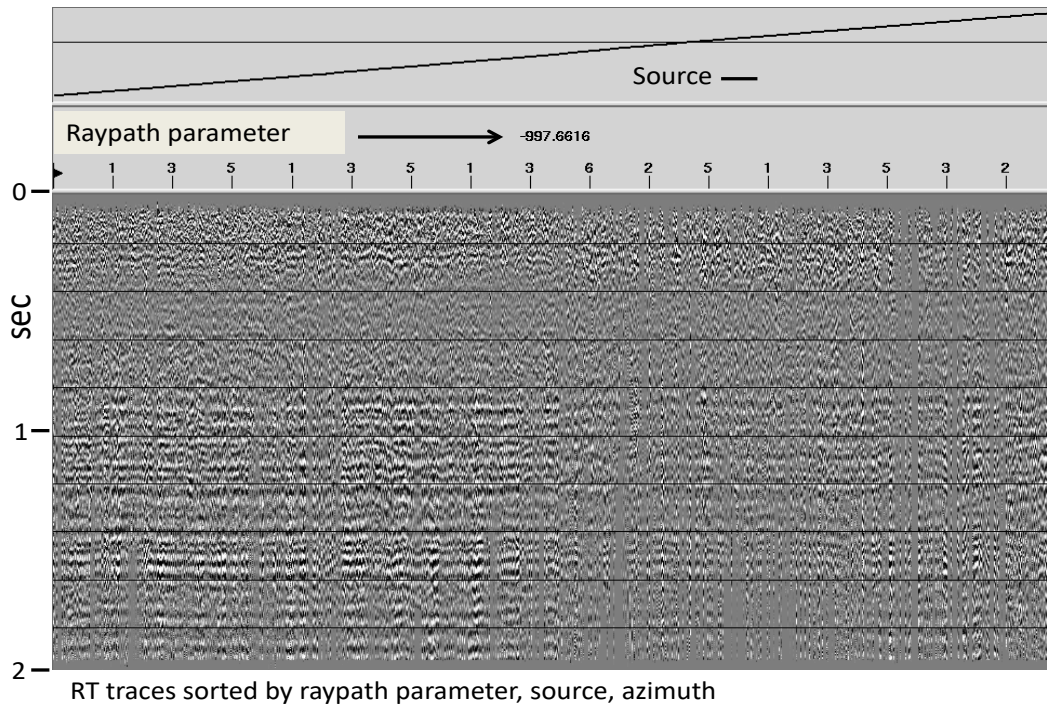


FIG. 17. The same vertical component Blackfoot traces as in Figure 16, for one common-ray-parameter gather, sorted by source, then azimuth.

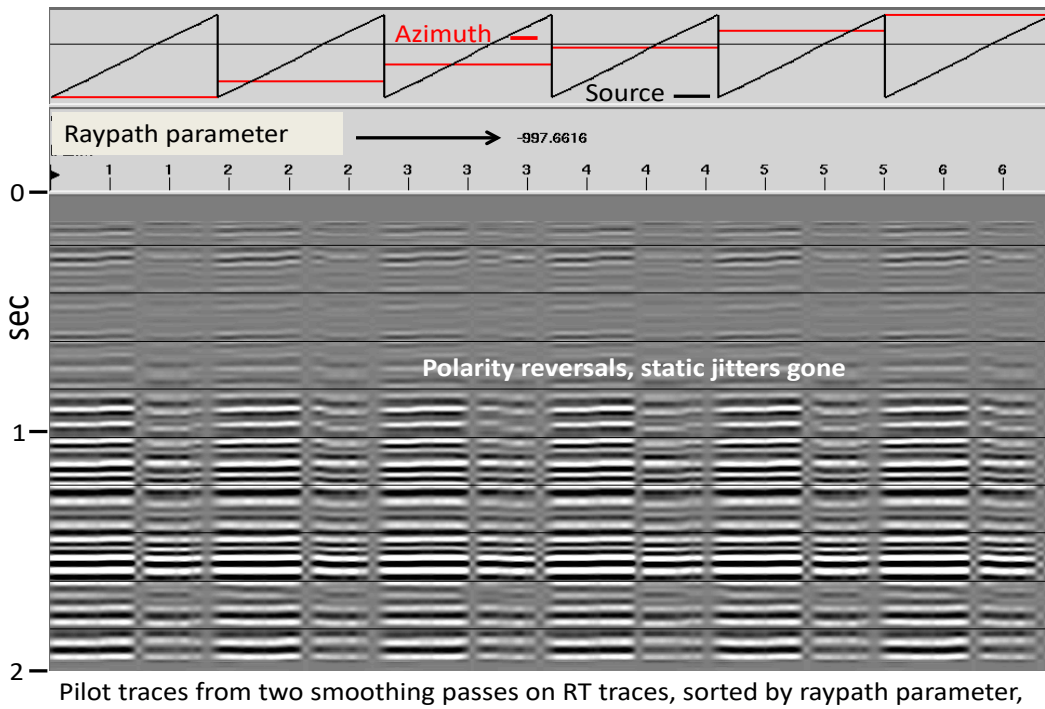


FIG. 18. Traces from Figure 16, for one common-ray-parameter, smoothed in both azimuth and source directions to form reference wavefield.

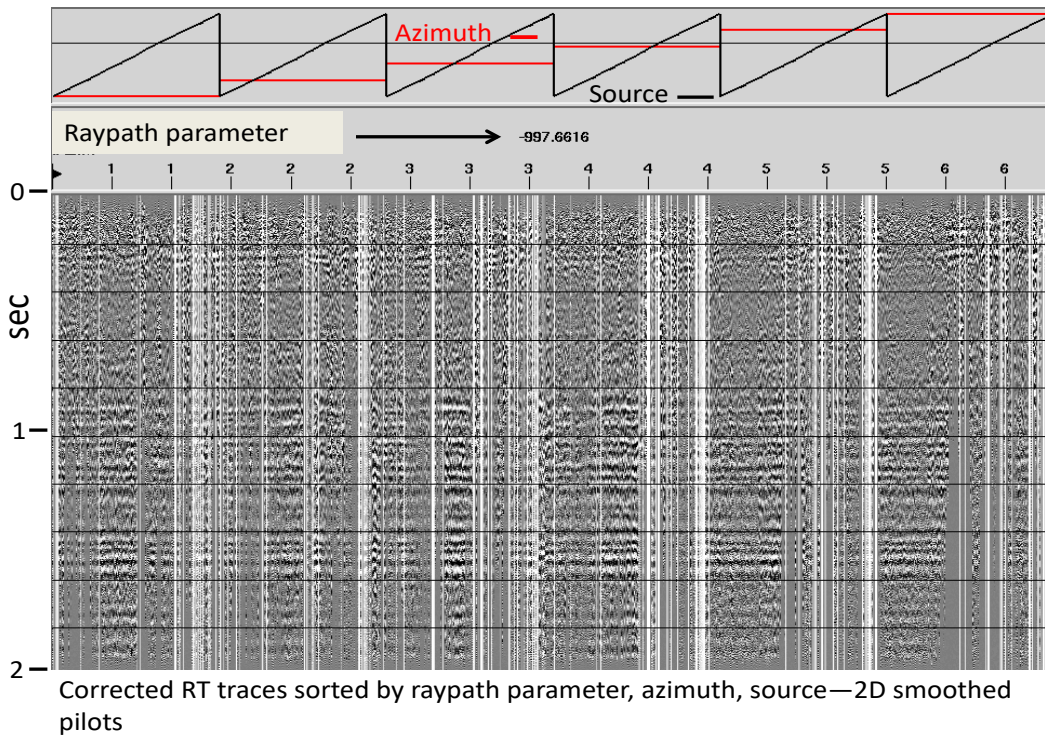


FIG. 19. Common-ray-parameter gather from Figure 16 after application of raypath interferometry.

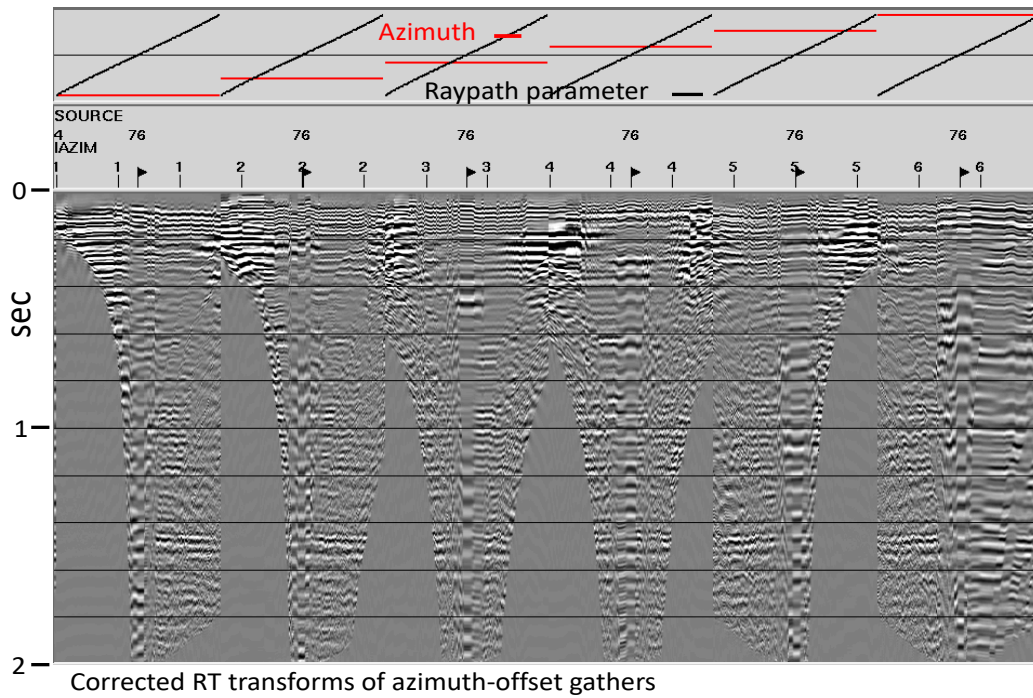


FIG. 20. RT Transforms of Figure 15 after application of raypath interferometry.

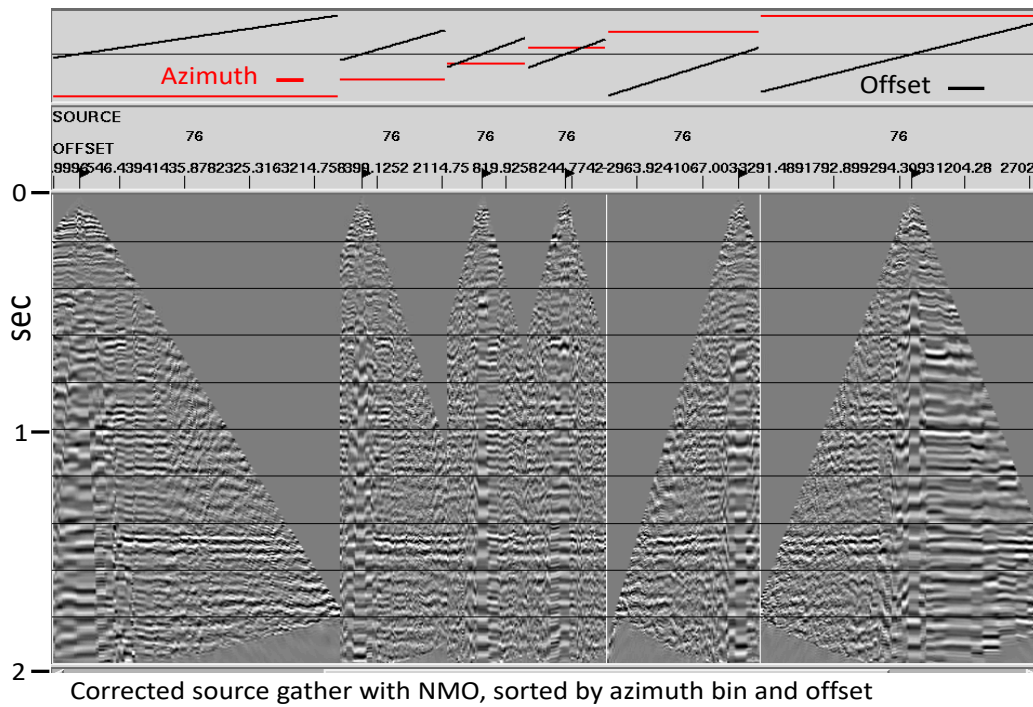


FIG. 21. Binned source gather of Figure 14 after application of raypath interferometry in the RT domain and inverse RT transform. Note that the offset distributions have all been forced to be linear by the inadequate inverse RT Transform, which was only designed to handle 2D geometry.

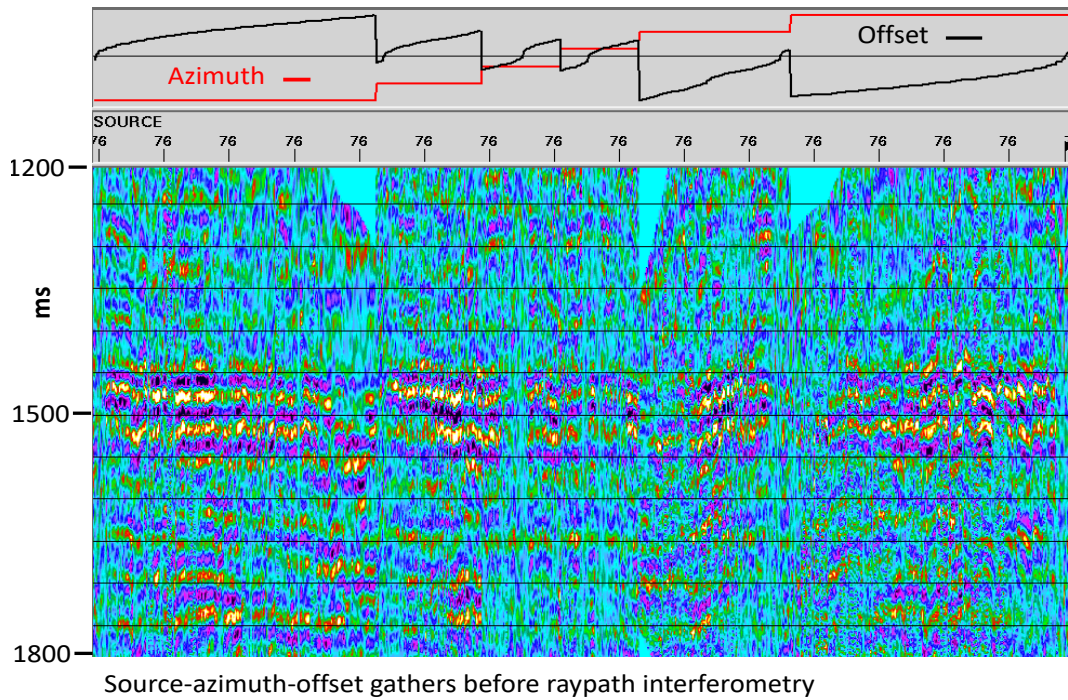


FIG. 22. Windowed portion of the input source-azimuth-offset vertical component gather for Blackfoot source 76 before raypath interferometry.

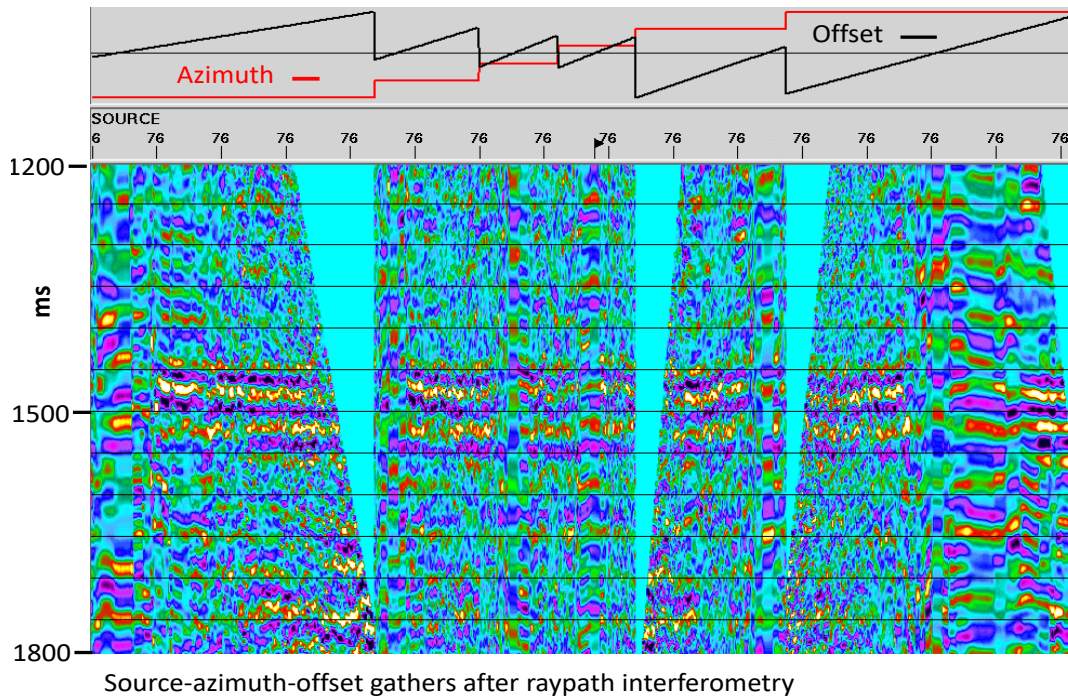
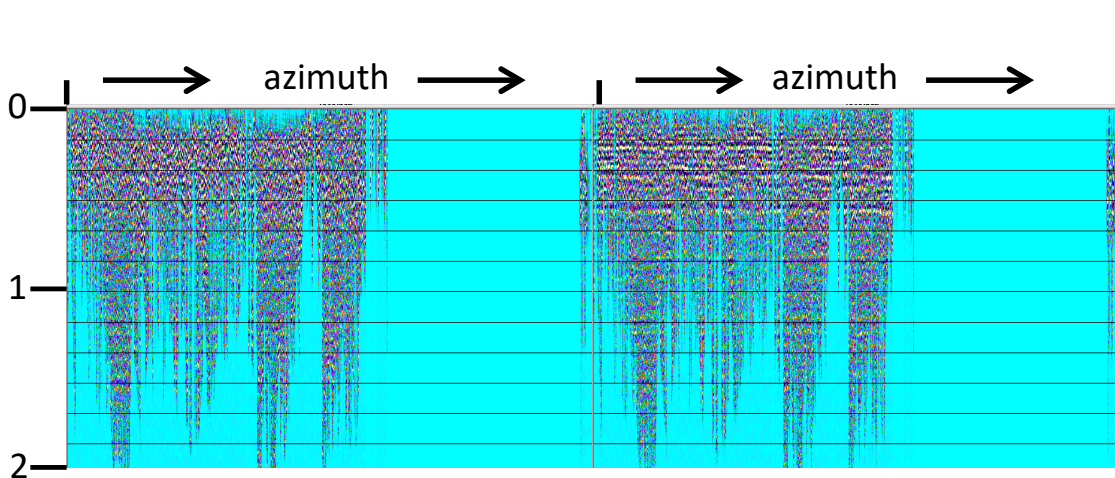
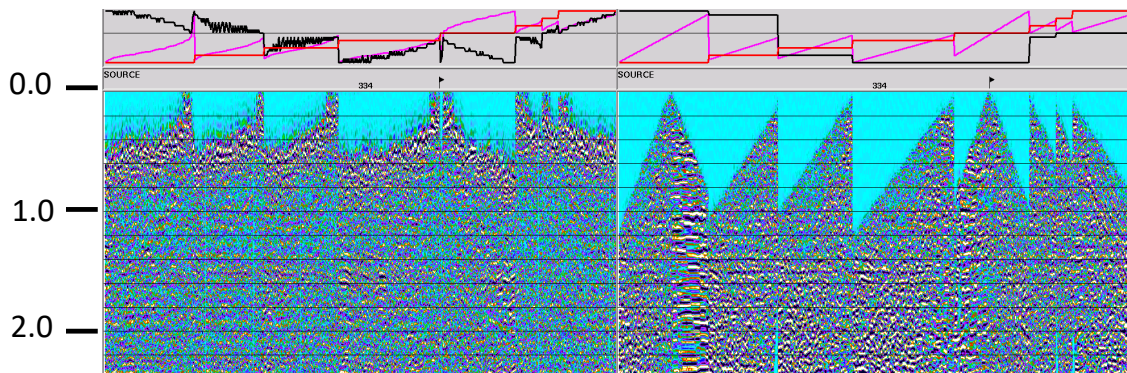


FIG. 23. Windowed portion of the source-azimuth-offset vertical component gather for Blackfoot source 76 after raypath interferometry. In spite of the distorted offset distributions, modest improvements in event coherence and flatness can be seen, compared with Figure 22.



Common-ray-parameter gather before (left) and after (right) raypath interferometry

FIG 24. Common-ray-parameter gather for the inline radial component of Blackfoot 3D 3C survey before raypath interferometry (left) and after raypath interferometry (right). Improved event coherence and alignment are obvious.



PS source gathers before (left) and after (right) raypath interferometry—while events are flattened, geometry is not properly restored

FIG. 25. Inline radial source gather for Blackfoot 3D 3C survey, sorted by azimuth then offset, before raypath interferometry (left) and after raypath interferometry (right). Improved event coherence is observed, but distorted offset distributions prevent further processing.

3D raypath interferometry—Tau-P Transform

We originally incorporated the RT Transform into the raypath interferometry technique because of its exact amplitude invertibility and lateral resolution. As shown above, however, the algorithm we implemented does not properly recover the original trace headers of the input trace gather, but instead substitutes linearly interpolated values for a key header, the source-receiver offset. In the case of 2D data, this approximation is quite good, but for 3D data, where the distribution of offsets deviates considerably from

linearity, unacceptable errors are introduced into the inversion of the RT Transform. Cova et al (2014c, 2015a, 2015b, 2016, 2017) showed, however, that the Tau-P Transform could be used instead of the RT Transform, and as a commercial software module, it properly recovers all trace headers from the input trace gather for inversion of the transform. The main disadvantage of using the Tau-P Transform is that in order to preserve the lateral resolution of the original input trace gather, many projection slices must be created in the forward transform, between rather large values of the ray-parameter (slowness). This dramatically increases the required storage for the Tau-P Transform, which can be two orders of magnitude more than that required for the input trace gather. For 2D data sets, this is generally of little consequence, but the sheer size of most 3D data sets means that substantial storage must be available to store the intermediate Tau-P files. For example, Figure 26 shows the Tau-P Transform computed from the traces in one azimuth bin for one of the vertical component shot gathers from the Blackfoot survey. In this particular example, the Tau-P Transform requires about 90 times the storage of the input traces.

Figure 27 compares an original common-azimuth ensemble of traces from one shot gather (a), with the result of the forward/inverse RT Transform (b), and the result of the forward/inverse Tau-P Transform (c), using the same Tau-P parameters used to create the transform in Figure 26. In all cases, the source-receiver offsets are plotted above in red. We can readily see the data distortion caused by the imposition of a linear offset distribution in the RT Transform in (b), and we can also see, in (c), that the Tau-P Transform preserves the lateral trace-to-trace detail of the original gather. Figures 28 and 29 illustrate how we lose lateral resolution if we reduce the min and max slowness values for the Tau-P Transform in order to reduce storage. The comparable reduced storage limits are shown in yellow on Figure 26. Neither of these parameter settings would be considered acceptable, since the obvious lateral smearing would affect the surface locations at which appropriate corrections can be derived and applied.

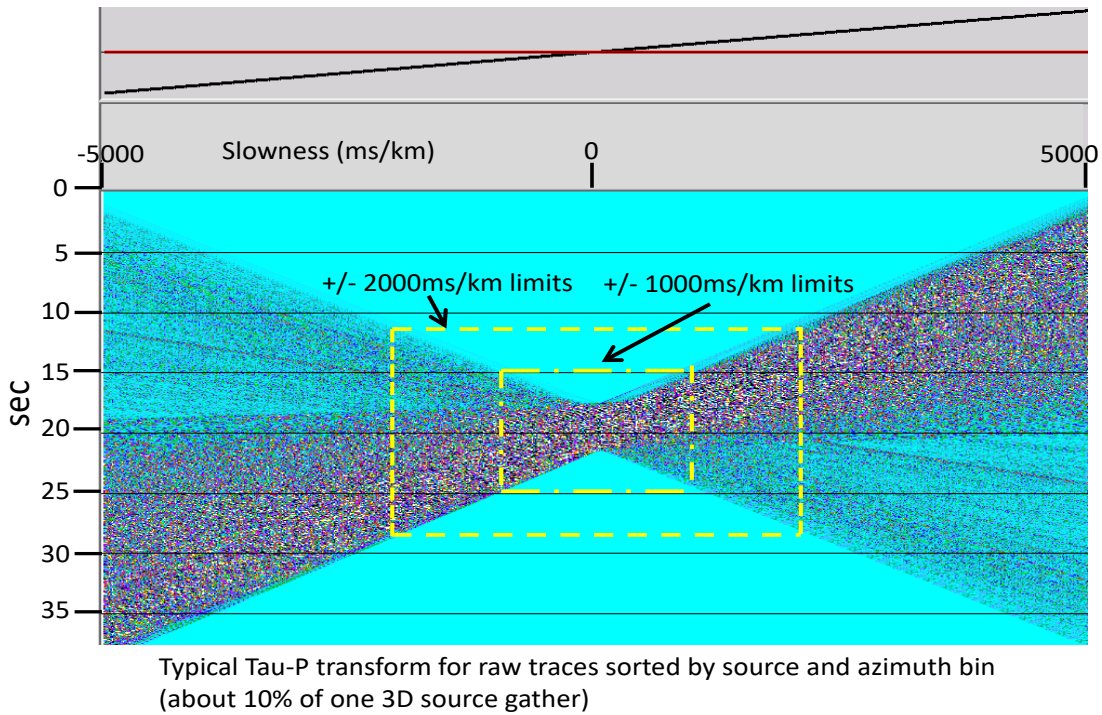


FIG. 26. Typical Tau-P Transform for one bin of a vertical component source gather from Blackfoot. A single bin is about 10% of the data for one 3D source gather. This figure illustrates that as the required lateral resolution of the Tau-P transform increases, the data storage requirement increases dramatically. Roughly, storage increases as the square of the slowness.

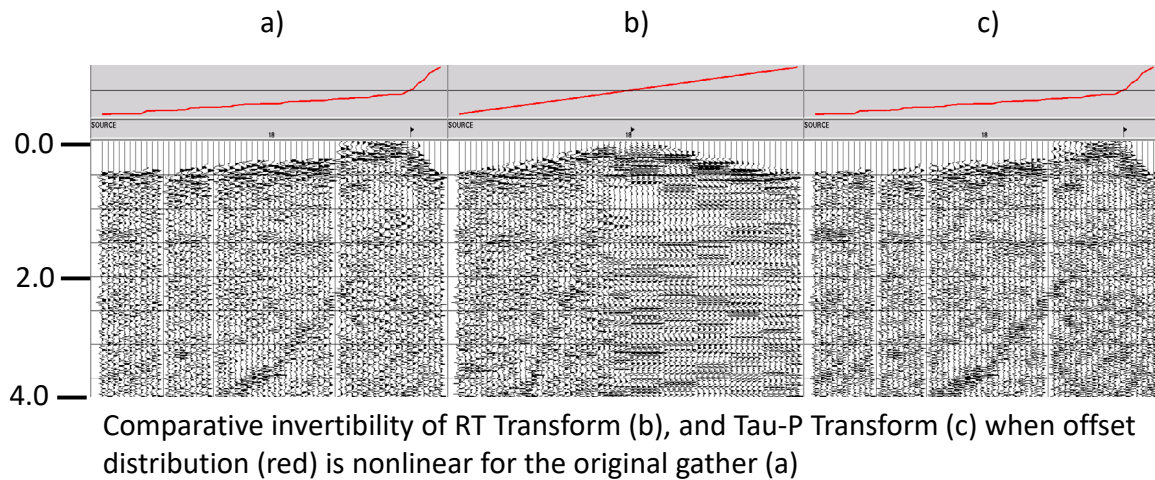


FIG. 27. PS (inline radial component) gather for one azimuth bin from Blackfoot 3D 3C. a)—original trace gather. b)—trace gather after forward/inverse RT Transform. c)—trace gather after forward/inverse Tau-P Transform with proper ray-parameter limits (slowness range is -5000ms/km to 5000ms/km). The RT inverse linearizes the offset distribution, thus distorting the data themselves and preventing a proper inverse. Tau-P inverse, on the other hand, properly recovers offset values.

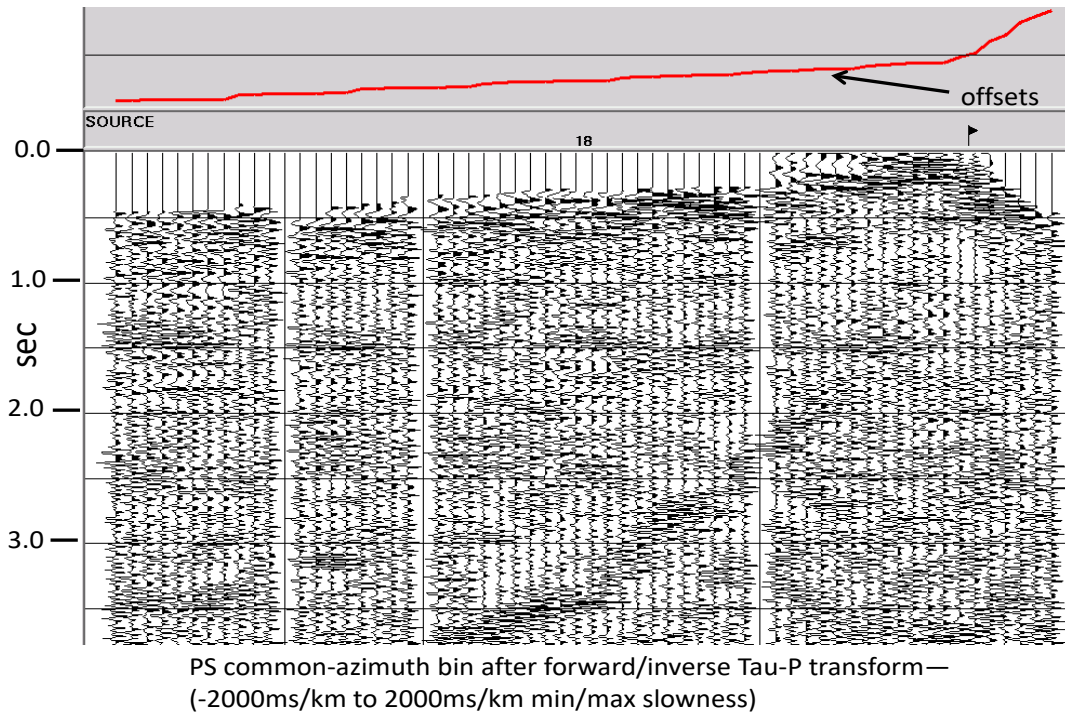


FIG. 28. Common-azimuth trace gather after forward/inverse Tau-P Transform with reduced slowness range = -2000ms/km to 2000ms/km. While required storage is much less (Figure 26), lateral resolution is compromised.

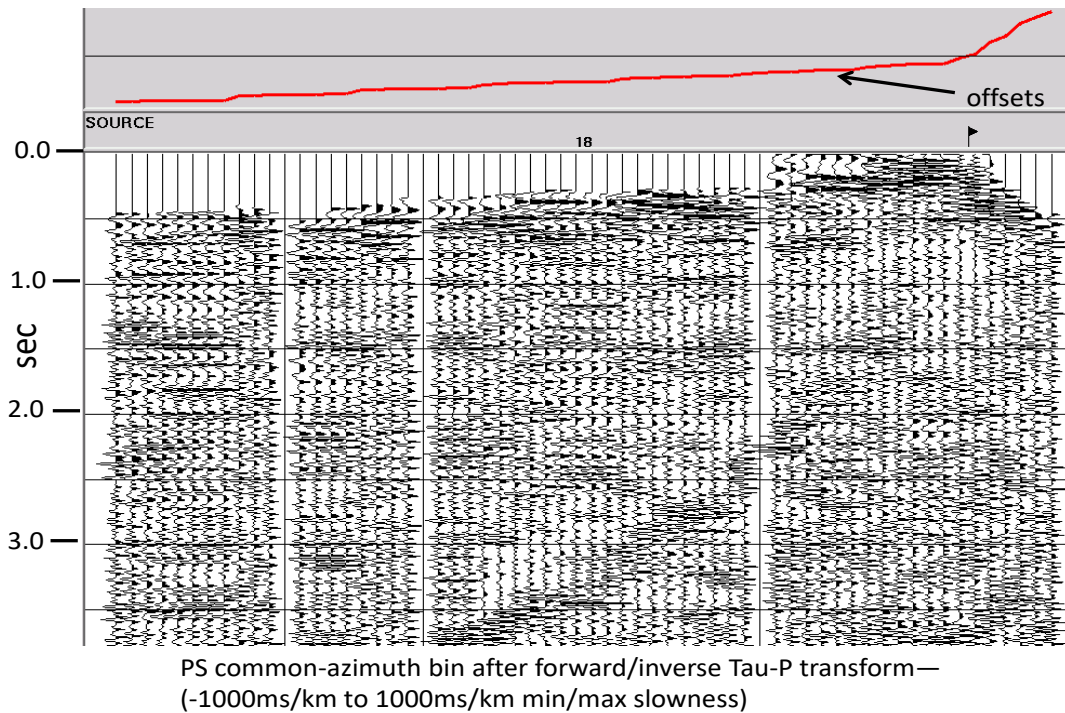
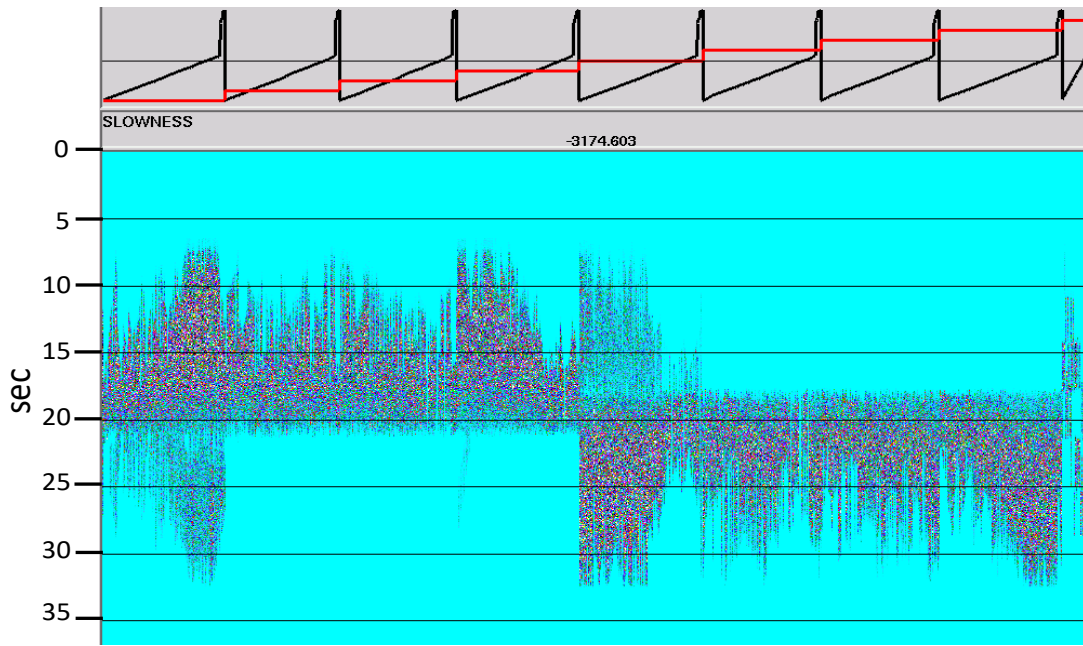


FIG. 29. Common-azimuth trace gather after forward/inverse Tau-P Transform with considerably reduced slowness range = -1000ms/km to 1000ms/km. Storage is even less than for Figure 28 (Figure 26), but lateral resolution is completely unacceptable.

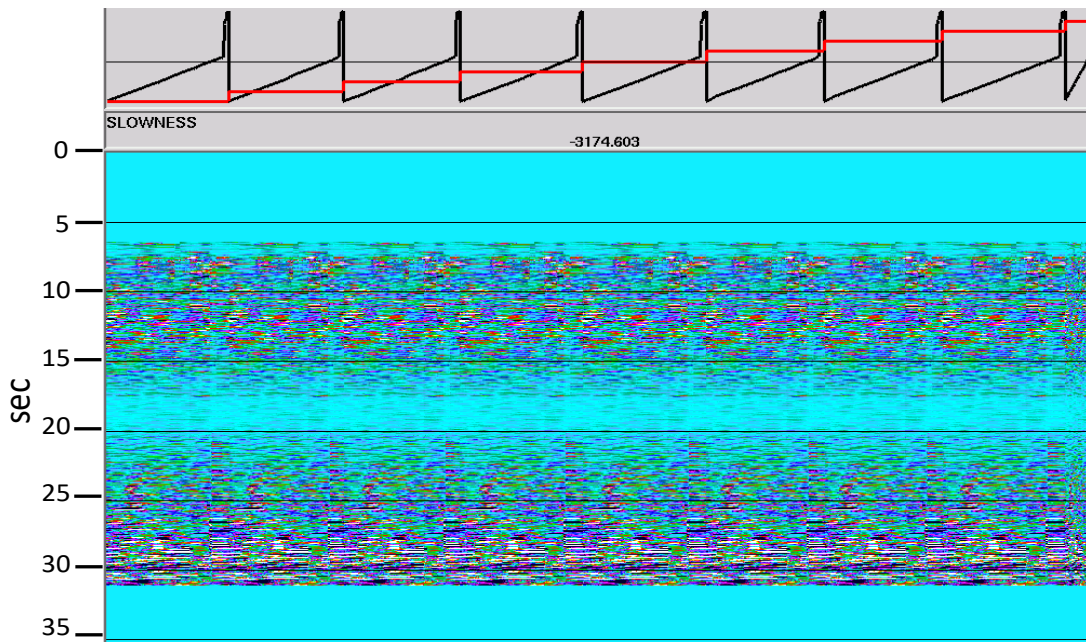
PP raypath interferometry using the Tau-P Transform

To apply 3D raypath interferometry to the PP (vertical) component of the Blackfoot 3D 3C survey, we began with the same binning scheme described earlier for the RT domain: traces sorted by source/azimuth-bin/offset. We applied the Tau-P Transform to each azimuth bin of traces within each source gather, then sorted the entire data set into common-ray-parameter trace gathers, of which one is displayed in Figure 30, with azimuth bin (red) and source number(black) plotted along the top. From this plot, it is difficult to appreciate the amount of data represented; there are approximately 20,000 traces, each 37,000ms in length, and this common-ray-parameter gather is only one of 631 representing the entire Blackfoot survey. The sheer size of all such ensembles leads to significant storage/retrieval and execution times for all the operations of raypath interferometry. Figure 31 shows the reference wavefield ensemble created from the data in Figure 30 by smoothing in 2 directions, and Figure 32 shows a panel of paired reference/raw traces for cross-correlation (at a different ray-parameter). Because of the length of the traces, the cross-correlations require significant computation time. Figure 33 shows the full set of ‘conditioned’ correlation functions computed from the common-ray-parameter trace panel in Figure 32. On this scale, the functions appear to be mostly zero-shift; but this is an visual illusion, as we can see from a greatly expanded zoom view in Figure 34. Lest we get the impression that these random-appearing functions are unlikely to improve the coherence of the raw common-ray-parameter traces, we show in Figure 35 a small portion (approx 2%) of the common-ray-parameter ensemble for ray-parameter -4841 before application of interferometry, and in Figure 36 the same portion after application of the inverse filters derived from the surface functions shown in Figure 33. The improved event continuity is visible at all levels.



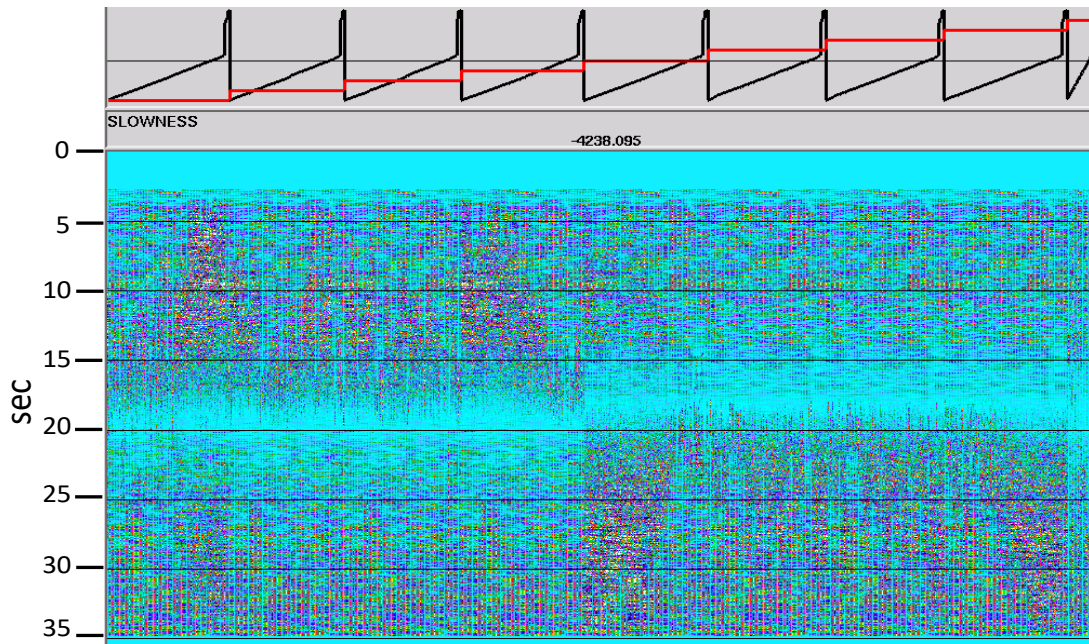
Typical common-ray panel

FIG. 30. A typical common-ray-parameter gather in the Tau-P domain for the vertical component of the Blackfoot 3D 3C survey. This gather, with over 20,000 traces, each 37,000ms in length is only one of 631 gathers for this data set, thus illustrating the very large storage issue created by using the Tau-P domain for common-raypath processing.



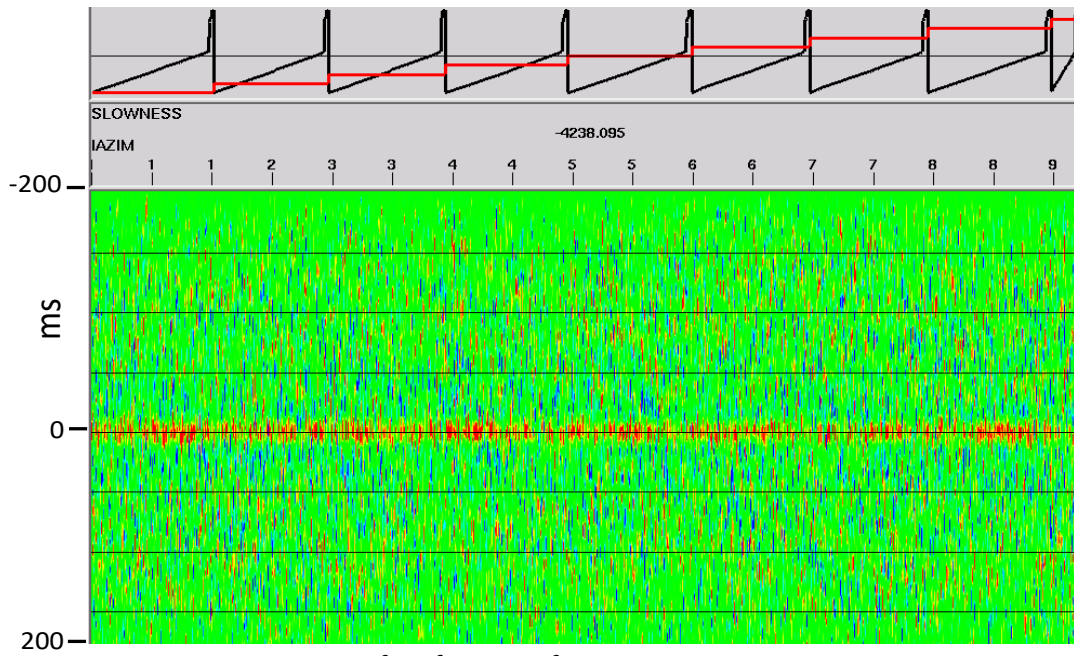
Reference wavefield for common-ray panel, smoothed in 2D

FIG 31. Reference wavefield gather created for the common-ray-parameter gather in Figure 29 by smoothing in two directions.



An example of common-ray trace pairs for X-correlation

FIG. 32. Paired traces (raw trace and reference trace) for a common-ray-parameter gather for the vertical component of the Blackfoot 3D 3C survey.



Surface functions for PS common-ray traces

FIG. 33. Surface functions, consisting of the cross-correlations of the trace pairs in Figure 32, which have been conditioned. Although the functions seem to be predominantly centred on zero, the expanded view of a portion of these functions, shown in Figure 34, shows that the horizontal scale of Figure 33 is too compressed to show the details.

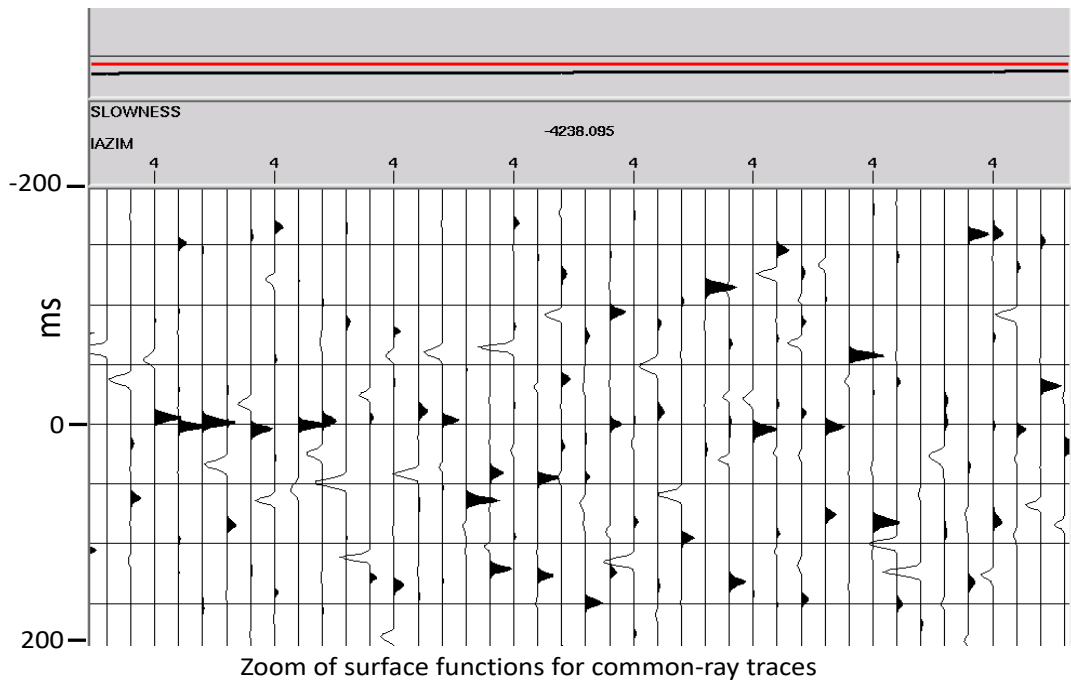
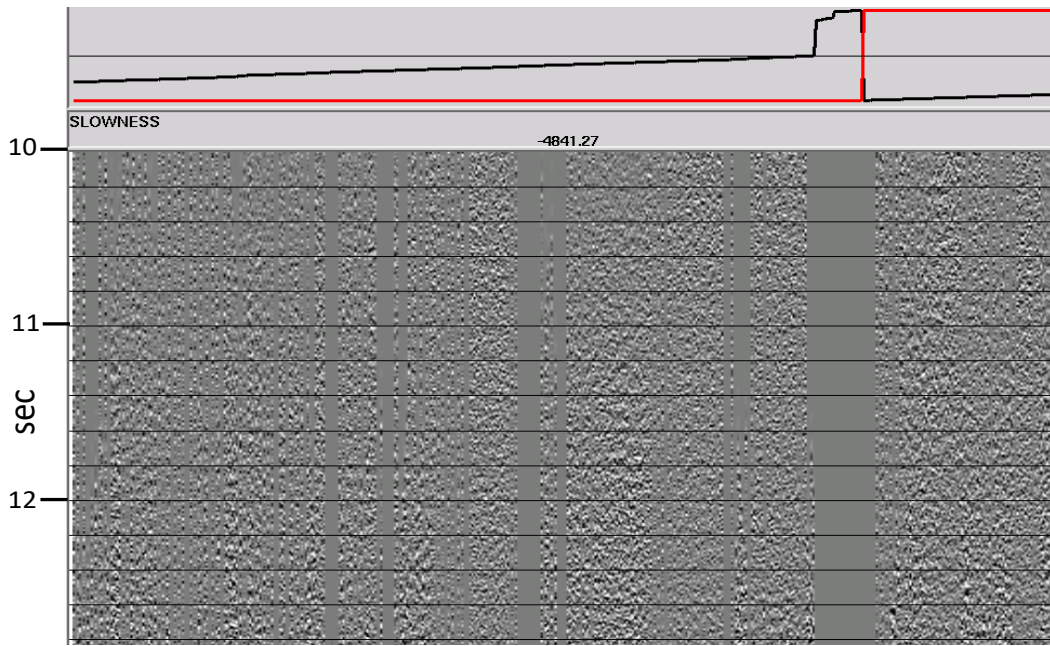
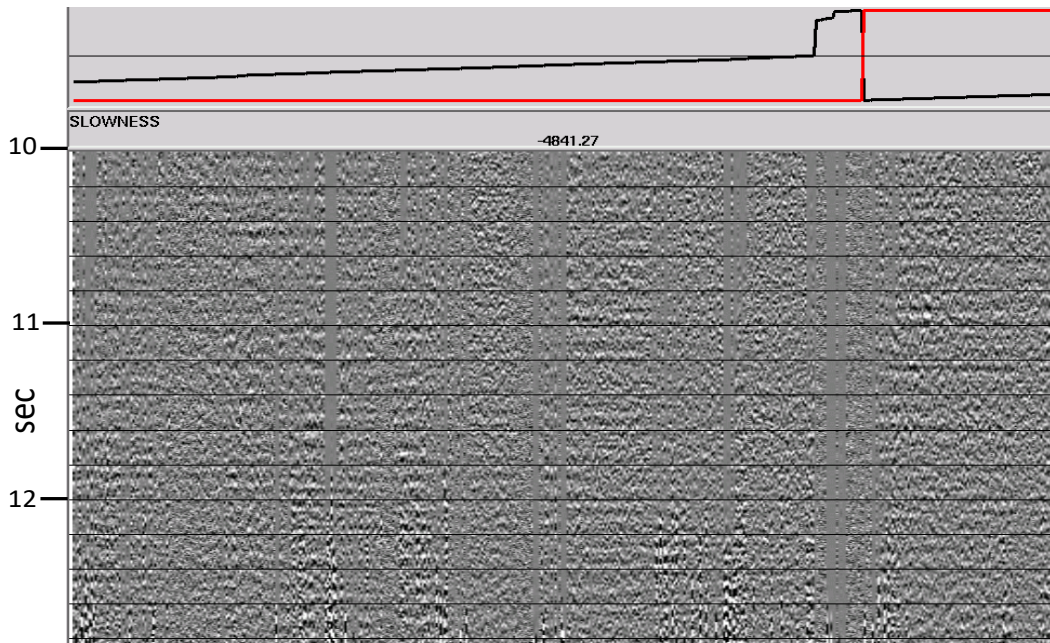


FIG. 34. Expanded view of a small portion of the surface functions in Figure 33, showing that many of the functions will apply significant time-shifts/phase-corrections to the traces to which they're applied.



Portion of a common-ray Tau-P gather before interferometry

FIG. 35. Small portion (about 2%) of a Blackfoot vertical component common-ray-parameter Tau-P trace gather before raypath interferometry correction.



Portion of a common-ray Tau-P gather after interferometry

FIG. 36. The common-ray-parameter traces from Figure 35 after correction by raypath interferometry.

The proof is in the stack

It is one thing to show improved coherence of events on common-ray-parameter ensembles, and another to complete the process and invert the ‘corrected’ data back to the original X/T gathers for CMP imaging. Our first attempt failed due to lack of sufficient storage resources on the computing system; but a subsequent attempt succeeded in producing a full set of PP (vertical component) source gathers for the Blackfoot survey with 3D raypath interferometry used to apply surface corrections. Figure 37 shows the complete source/receiver-line ensemble for source point 336 of the Blackfoot PP survey, with NMO applied, but no surface corrections, while Figure 38 shows the same ensemble after application of raypath interferometry. While the various reflection events are not perfectly flat, we observe a general improvement in event continuity and flatness, particularly for the shorter wavelength deviations we typically associate with ‘statics’. The traces in the source ensembles are in a completely different order than when they were transformed to the common-ray-parameter domain, so the appearance of improved event coherence in these ensembles is evidence that raypath interferometry is, in fact, applying the surface corrections we need.

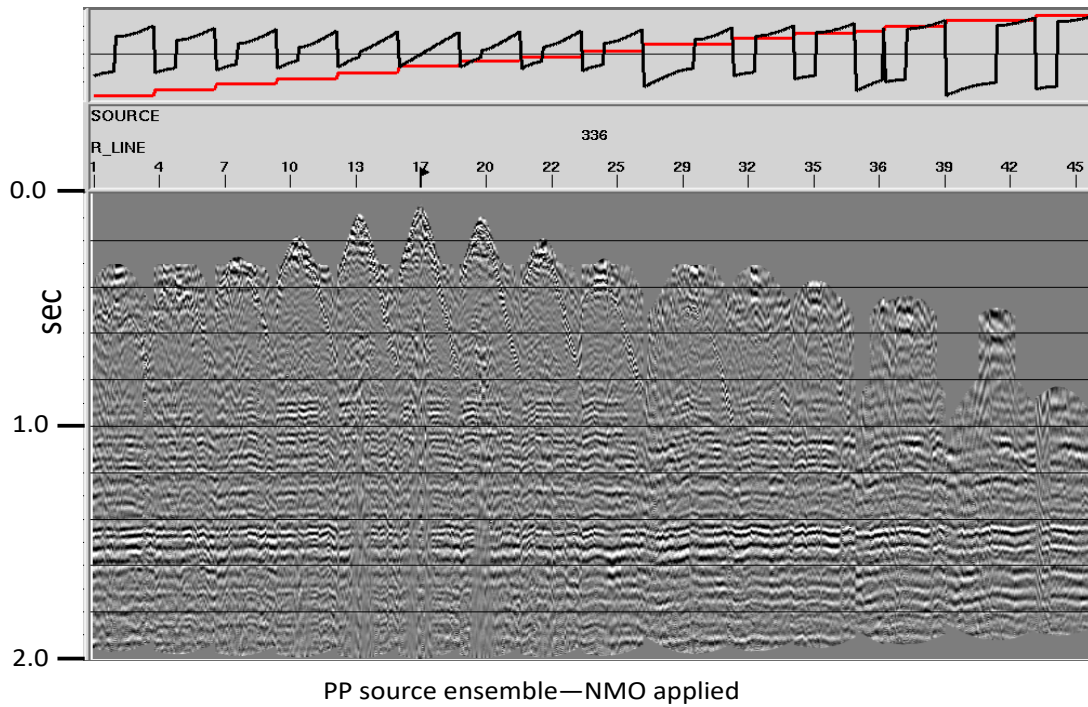


FIG. 37. Blackfoot vertical component source gather, for source point 336, sorted by receiver lines, with NMO applied, no statics.

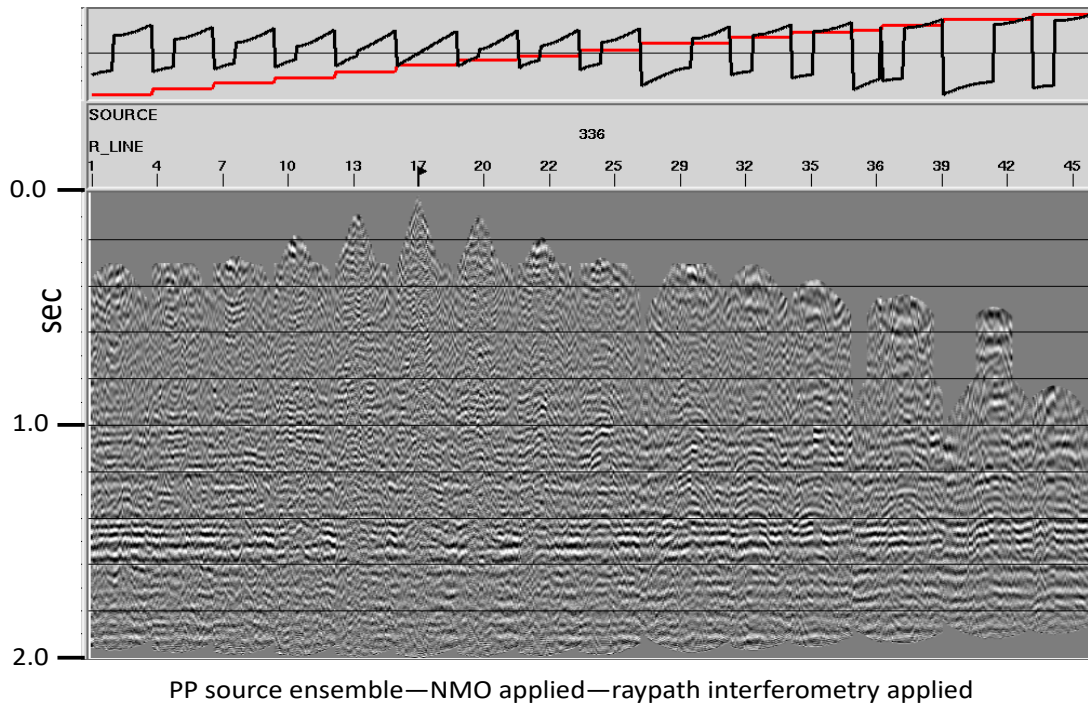


FIG. 38. Blackfoot vertical component source gather from Figure 37, with NMO applied, after application of raypath interferometry.

The next test of our success was to examine CMP-stacked data before and after raypath interferometry. To do this comparison, we stacked the data in their originally

assigned 3D bins and compared 2D slices of the 3D stack volume, both in the original inline direction, and in the crossline direction to check that our surface corrections are truly 3D. Figure 39 shows a compressed view of six neighboring, parallel 2D inline slices of the 3D CMP-stacked data volume, with no statics or other surface corrections applied, while Figure 40 shows the same data, but after raypath interferometry. The visibly improved stack amplitudes and event coherence over much of the time range of the data is evidence of the success of raypath interferometry. Figures 41 and 42 compare two individual 2D CMP stack slices before and after raypath interferometry, as do Figures 43 and 44. In both of these comparisons, most events are stronger, flatter, and more coherent after raypath interferometry.

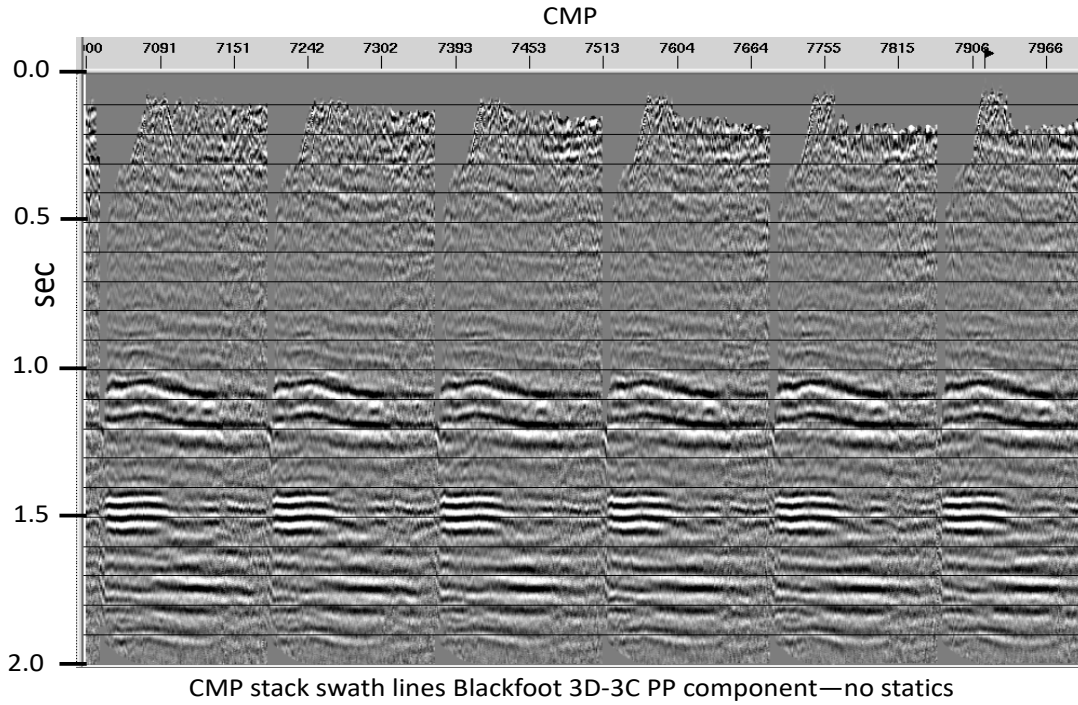


FIG. 39. Six CMP stacked vertical component lines from the Blackfoot 3D data volume—no statics applied. Inline direction.

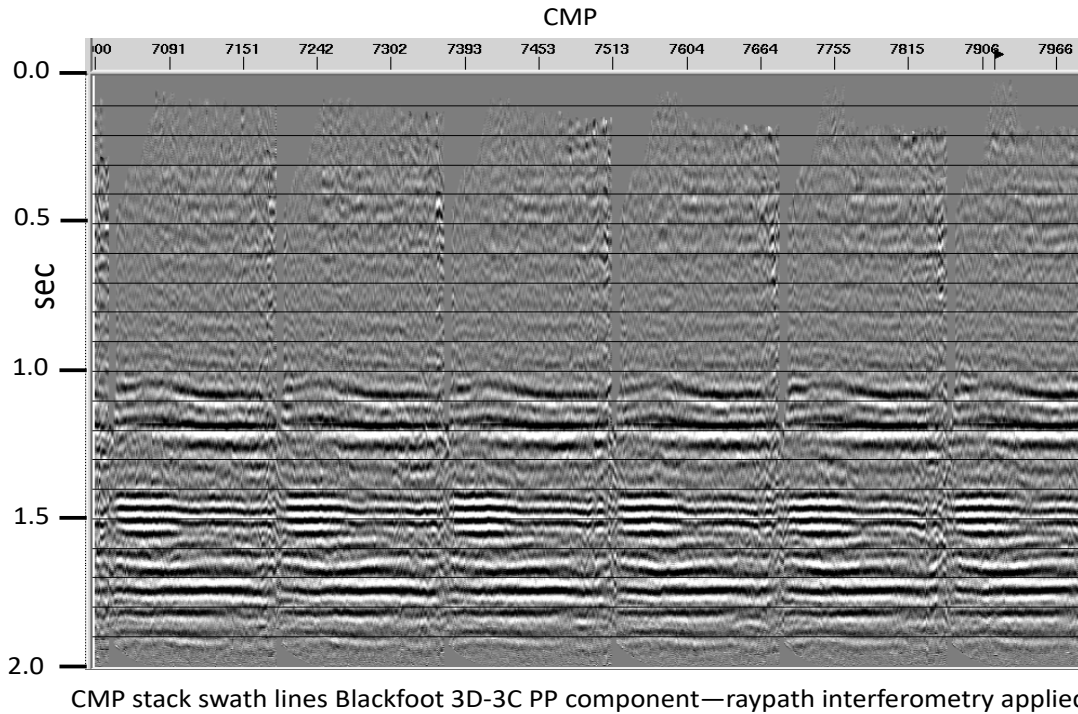


FIG. 40. Six CMP stacked vertical component lines from the Blackfoot 3D data volume—raypath interferometry applied. Inline direction.

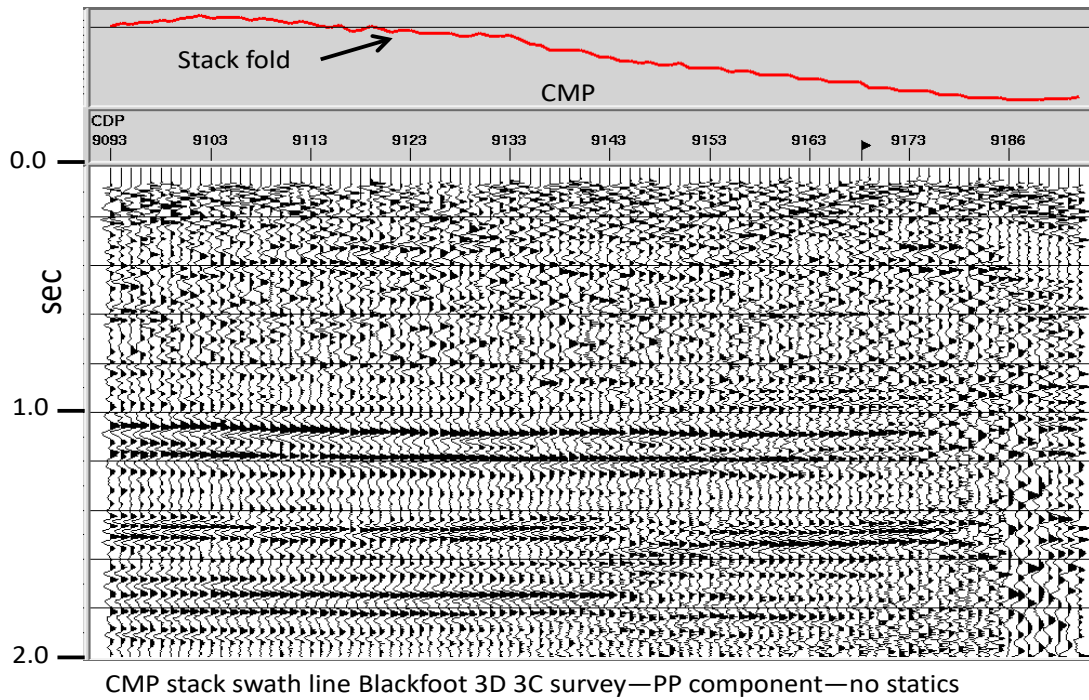


FIG. 41. Single CMP stack line from the Blackfoot 3D vertical component data volume—no statics applied. Inline direction.

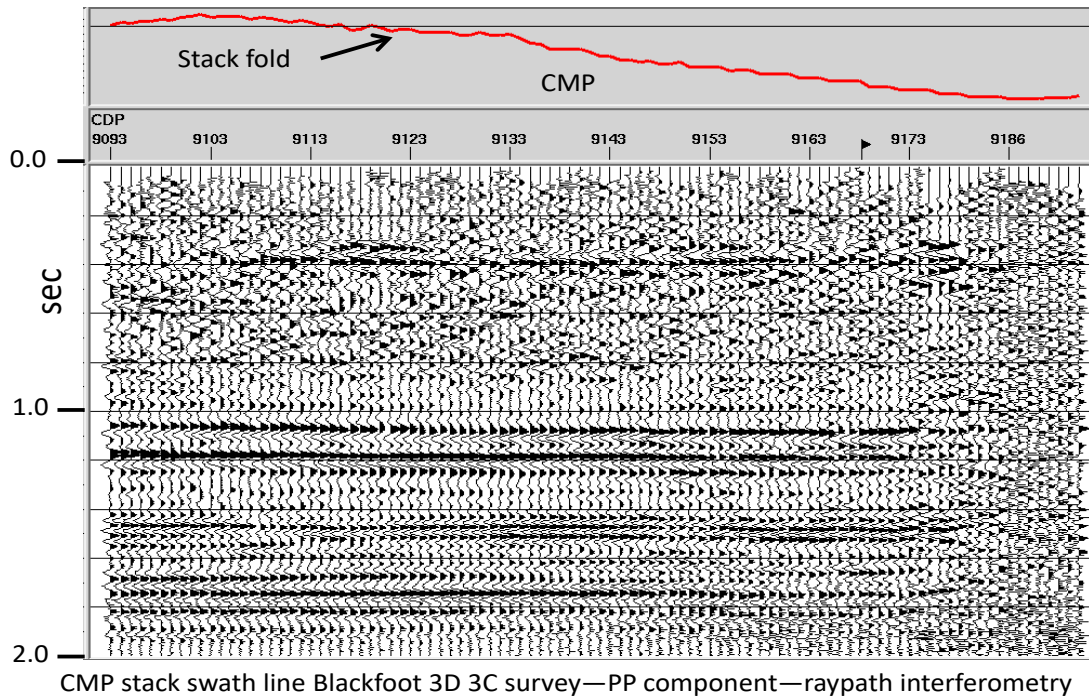


FIG. 42 Single CMP stack line from the Blackfoot 3D vertical component data volume—raypath interferometry applied. Inline direction.

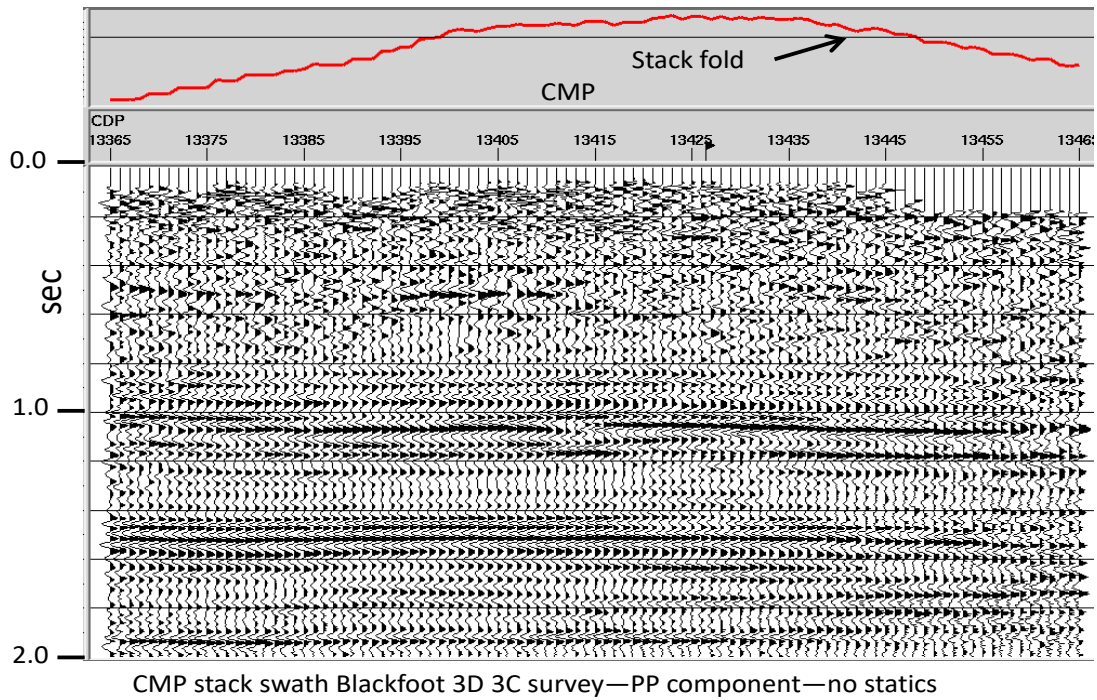


FIG. 43. Single CMP stack line from the Blackfoot vertical component data volume—no statics applied. Inline direction.

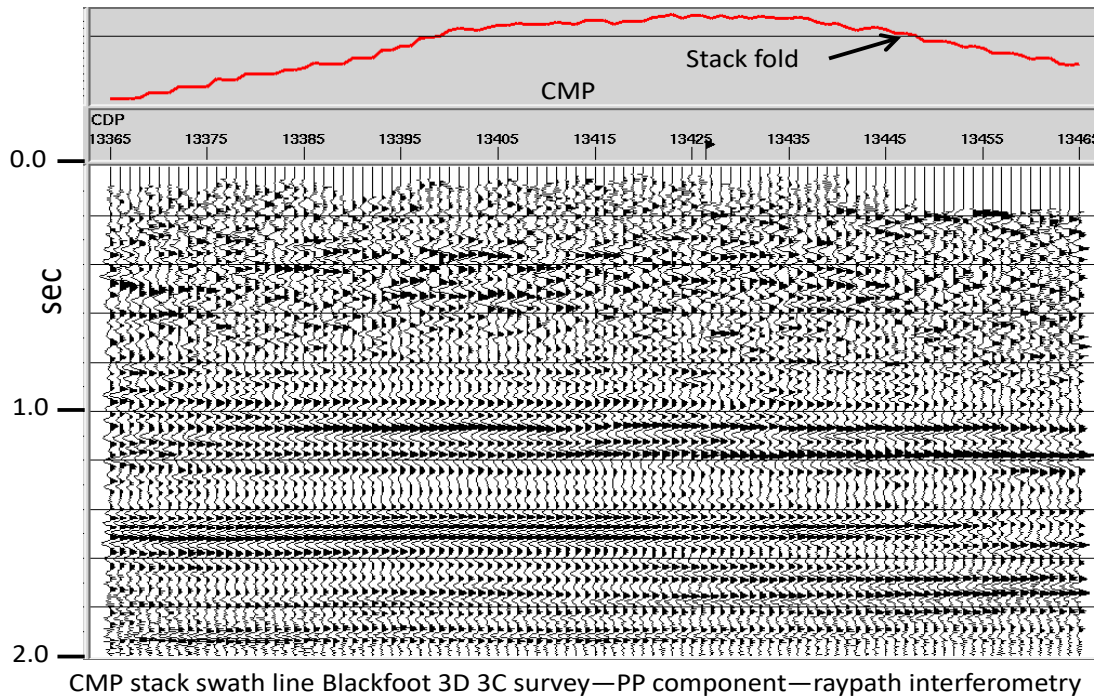


FIG. 44. Single CMP stack line from the Blackfoot vertical component 3D data volume—raypath interferometry applied. Inline direction.

To verify that raypath interferometry is applying surface corrections that are truly 3D, we show a crossline 2D CMP stack slice (normal to the inline stack slices above) in Figure 45, with no statics or surface corrections, and in Figure 46, the same data after raypath interferometry.

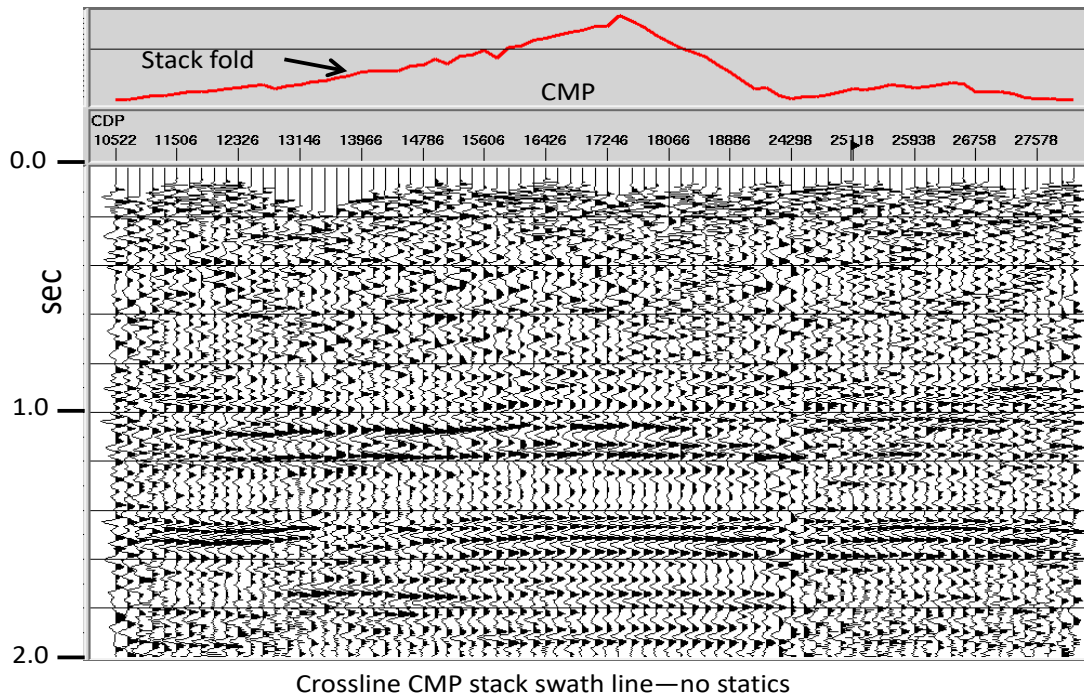


FIG. 45. Single CMP stack line from the Blackfoot vertical component 3D data volume—no statics applied. Crossline direction.

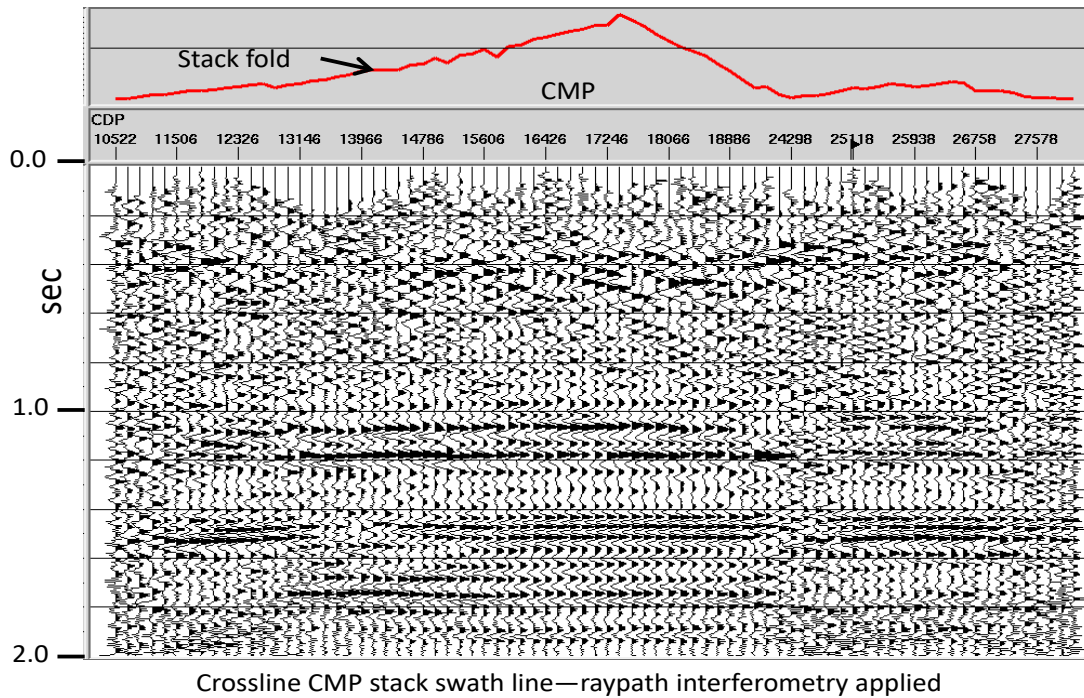


FIG. 46. Single CMP stack line from the Blackfoot vertical component 3D data volume—raypath interferometry applied. Crossline direction

DISCUSSION

We have demonstrated one way of implementing raypath interferometry for 3D seismic data. In order to relate localized surface corrections to the 3D coordinates of seismic data, we elected to express a raypath-dependent surface function in coordinates of surface location (source number), raypath angle, and raypath azimuth. This necessitates creating new trace headers for the input seismic traces that include signed source-receiver offset and source-receiver azimuth, as well as an azimuth bin number. Since the usual acquisition geometry for land 3D seismic data is based on Cartesian coordinates, seismic trace gathers from bins based on those coordinates are usually well-populated and relatively uniformly spaced. Forming trace gathers based on source-receiver offset and azimuth bins, however, introduces a trade-off between adequate trace population and regular offset distribution within the individual azimuth bins. In order to ensure both adequate trace population and regular offset distribution, the azimuth bins often need to be uncomfortably wide, so raypaths in these bins are not as coplanar as the common-raypath model assumes. Fortunately, the azimuthal component of near-surface corrections appears to vary only very slowly with azimuth, so that relatively wide azimuths can be justified.

In addition to the awkwardness of azimuth binning, a closely related issue is the uniformity of the distribution of source-receiver offsets within each bin. This is of concern primarily when using the 2D Radial Trace Transform to move the input data from the X/T domain to a raypath domain, since our current Radial Trace Transform does not handle geometric trace headers properly. Because of this deficiency, we cannot properly invert Radial Trace Transforms to re-create output traces with the same geometry as their corresponding input traces; and we can therefore not complete the processing of a 3D data volume after raypath interferometry. For this reason, we choose the Tau-P Transform to convert X/T data to the raypath domain and back, even though this transform has potential resolution/invertibility issues and requires a very large file space for intermediate files.

We have demonstrated improved event coherence and continuity for both PP and PS data from the Blackfoot survey, when comparing raw trace gathers with those subjected to interferometry, when using the RT transform; but only when we use the Tau-P Transform have we been able to complete the processing on the 3D data volume. Hence we showed some corrected PP source gathers as well as several inline and crossline swaths of CMP stacked traces from the 3D data volume. For the PP data, it is evident that the raypath interferometry was a success, and we can only assume that the same process applied to the PS data would also be successful.

Because raypath interferometry is a relatively tedious exercise, we do not recommend it for routine application to 3D PP data, particularly if conventional static corrections can be successfully applied. The process might be worth applying to PS data, however, since statics for these data are nonstationary, and surface-consistent static solutions tend to correct for events at a particular depth, and don't work so well for events shallower or deeper.

ACKNOWLEDGEMENTS

The author gratefully acknowledges financial support from CREWES sponsors, as well as funds from NSERC. Discussions with CREWES staff, particularly R. Cova and K. Innanen are also gratefully acknowledged.

REFERENCES

- Claerbout, J.F., 1983, Ground Roll and Radial Traces, Stanford Exploration Project Report, SEP-35, pp 43-53.
- Cova, R., Henley, D.C., and Innanen, K.A.H., 2013a, Non-stationary shear wave statics in the radial trace domain, CREWES Research Report, **25**.
- Cova, R., Henley, D.C., and Innanen, K.A.H., 2013b, An interferometric solution for raypath-consistent shear wave statics, CREWES Research Report, **25**.
- Cova, R., Henley, D.C., and Innanen, K.A.H., 2014a, Using ray-path domain interferometry to address non-stationary S-Wave statics, SEG Technical Program Expanded Abstracts 2014.
- Cova, R., Henley, D.C., and Innanen, K.A.H., 2014b, Inverting raypath dependent delay times to compute S-wave velocities in the near surface, CREWES Research Report, **26**.
- Cova, R., Henley, D.C., and Innanen, K.A.H., 2014c, Making shear wave statics actual statics using radial trace and tau-p transforms, CREWES Research Report, **26**.
- Cova, R., Wei, X., and Innanen, K.A.H., 2015a, Shear wave near-surface corrections in the tau-p domain: a case study, CREWES Research Report, **27**.
- Cova, R., Henley, D.C., and Innanen, K.A.H., 2015b, Addressing shear wave static corrections in the ray parameter domain: a non-stationary interferometric approach, SEG Technical Program Expanded Abstracts 2015.
- Cova, R., Wei, X., and Innanen, K.A.H., 2016, Converted-wave receiver statics in the tau-p domain, SEG Technical Program Expanded Abstracts 2016.
- Cova, R., Henley, D.C., Wei, X., and Innanen, K.A.H., 2017, Receiver-side near-surface corrections in the Tau-P domain: a raypath-consistent solution for converted wave processing, *Geophysics*, **82**, No. 2, pp U13-U23.
- Henley, D.C., 1999, Radial trace computational algorithms at CREWES, CREWES Research Report, **11**.
- Henley, D.C., 2008, Raypath interferometry: statics in difficult places, 2008, SEG Technical Program Expanded Abstracts 2008.
- Henley, D., 2012a, Interferometric application of static corrections: *Geophysics*, **77**, No. 1, Q1–Q13.
- Henley, D.C., 2012b, Interference and the art of static correction: raypath interferometry at Hussar, CREWES Research Report, **24**.
- Henley, D., 2014a, Static corrections via raypath interferometry: recent field experience: Geoconvention 2014, CSEG, Expanded abstracts 2014.
- Henley, D.C., 2014b, Raypath interferometry vs. conventional statics: recent field data and model comparisons, SEG Technical Program Expanded Abstracts 2014.
- Henley, D.C. 2014c, Through a glass darkly: improving raypath interferometry, CREWES Research Report, **26**.
- Henley, D.C., 2015, 3D or not 3D, that is the question: raypath interferometry in 3D processing, CREWES Research Report, **27**.
- Henley, D.C., 2016a, To boldly go into the next dimension: 3D raypath interferometry issues, CREWES Research Report—Volume **28**.
- Henley, D.C., 2016b, 3D or not 3D, that is the question: raypath interferometry in 3D processing, Geoconvention Expanded Abstracts, 2016.
- Henley, D.C., 2017, To boldly go into a new dimension: 3D raypath interferometry issues, Geoconvention Expanded Abstracts 2017.
- Simin, V., Harrison, M.P., and Lorentz, G.A., 1996. Processing the Blackfoot 3C-3D seismic survey. CREWES Research Report, **8**.